

UNIVERSITÉ LIBRE DE BRUXELLES

ULB

FACULTÉ DES SCIENCES

LABORATOIRE DE GLACIOLOGIE

Influence of the spatial variability of sub-shelf melting on Antarctic ice sheet sensitivity and response

Mémoire présenté par

HISLAIRE Sylvain

en vue de l'obtention du grade académique
de Master en Sciences et Gestion de l'Environnement,
Finalité Sciences de l'Environnement

Promoteur : Prof. Frank Pattyn

Année académique 2017 - 2018

Edge of the Dotson Ice Shelf (NASA/Jeremy Harbeck)
<https://flickr.com/photos/40635082@N07/30825385386>

Abstract

Melting beneath ice shelves is the largest sink of ice in the Antarctic mass budget. Ice shelves also stabilise the grounded ice through buttressing and limit sea level rise. Numerical models are needed to forecast the evolution of Antarctica, but coupling the ice sheet and the ocean requires extensive computational time. Parametrisations for subshelf melting exist but lack comprehensive intercomparison. In this thesis, a buoyant plume model parametrisation, a box model parametrisation and two polynomial melting laws compared against each other. Although the two formers are based on similar physics, they all yield substantially different melt rate and spatial distribution. They are then coupled to a one-dimensional ice stream model using parametrised buttressing. Ice sheet is shown to depend to a large extent on the shape of the shelves, which in turn evolve differently to the different melting laws.

.....

La fonte sous les plateformes de glace représente le plus important puits de glace dans le bilan de masse de l'Antarctique. Les plateformes de glace stabilisent la glace reposant sur un lit rocheux via un effet d'arc-boutant et limitent la hausse du niveau des mers. Pour prévoir l'évolution de l'Antarctique, des modèles numériques sont nécessaires, mais le couplage de la calotte glaciaire et de l'océan demandent beaucoup de temps de calcul. Des paramétrisations des modèles de fonte basale existent, mais elles n'ont pas encore été systématiquement intercomparées. Dans ce mémoire, une paramétrisation d'un modèle de panache d'eau saumâtre, une paramétrisation d'un modèle en boîte et deux lois polynomiales sont comparées. Bien que la physique sous-jacente soit similaire entre les deux premières, elles donnent toutes des résultats différents en grandeur et en distribution spatiale. Elles sont ensuite couplées à un modèle de courant de glace unidimensionnel avec un effet d'arc-boutant paramétré. La forme des plateformes de glace exerce un important contrôle sur la calotte, et évoluent de manière différente en fonction du modèle de fonte appliqué.

Contents

1	Introduction and state of the art	9
1.1	Subshelf melting	12
1.2	Marine Ice Sheet Instability	13
1.3	Ice-ocean coupling with buttressing	14
2	Models: Description	15
2.1	SSA ice flow model	15
2.2	Basal melt models	17
2.2.1	Plume model	18
2.2.2	Plume parametrization	19
2.2.3	Box parametrization (PICO)	24
2.2.4	Depth-dependant parametrisations	30
3	Models: Sensitivity analysis	32
3.1	SSA Ice flow model	32
3.1.1	Buttressing factor W	32
3.1.2	Viscosity parameter A	33
3.1.3	Friction coefficients c and m	34
3.2	Plume parametrisation	37
3.2.1	Dimensionless spatial coordinate	37

3.2.2	Melt rate	39
3.3	Box parametrisation	40
4	Coupling sheet-shelf and oceanic models	43
4.1	Implementation of the plume parametrization	44
4.1.1	Numerical scheme	44
4.1.2	Ad-hoc corrections	45
4.1.3	Melt-slope positive feedback	46
4.1.4	Flat shelf	51
4.2	Implementation of the box parametrization	51
5	Results and discussion	54
5.1	Comparison between the models	54
5.2	Grounding line retreat	59
6	Conclusion	64

List of Figures

2.1	Dimensionless melt curve $\hat{M}(\hat{X})$, plume parametrisation	20
2.2	Sensitivity of $\delta_T(\alpha)$ and $g_T(\alpha)$ to slope, plume parametrisation	21
2.3	Relation between basal depth, dimensionless variables and melt rate, plume parametrisation	23
2.4	Comparison between mean melt and melt over the first box for semi-circular and rectangular shelves, box parametrisation	27
2.5	The four parametrisations used in this thesis	30
3.1	Influence of buttressing factor W	33
3.2	Dependence of ice viscosity on temperature	34
3.3	Influence of viscosity parameter A	35
3.4	Influence of friction parameter c	35
3.5	Close-up on the grounding line for 4 sets of W, A, m, c	36
3.6	\hat{X} and \hat{M} against ocean temperature, plume parametrisation	37
3.7	Melt rate sensitivity to depth, slope and temperature	39
3.8	Sensitivity of the box parametrisation to overturning coefficient, turbulent exchange coefficient, and basin width, box parametrisation	41
3.9	Distribution of melt as a function of the maximum number of boxes, box parametrisation	42
4.1	Peak at the grounding line and wiggles near the shelf front, plume parametrisation	45

4.2	Shelf profile and corresponding melt rate for $\alpha = \alpha $ and $\alpha = \max(\alpha, 0)$ after 10 years, plume parametrisation	47
4.3	Steady-state profile and melt distribution at $\Delta x = 2\text{km}$ at $T_a = T_f^{\text{surf}} + 1^\circ\text{C}$, plume parametrisation	48
4.4	Different implementations of the saturation of effective slope, plume parametrisation	49
4.5	Melt rate below the Pine Island Glacier with logarithmic saturation of slope, plume parametrisation	50
4.6	Steady-state changes between average and upgraded resolution, box parametrisation	52
4.7	Sensitivity of grounding line retreat and initial and final mean melt rates as functions of number of boxes, box parametrisation	53
5.1	RMSD of four different statistics between the plume and the box parametrisations	55
5.2	Comparison between the mean melt rate and maximum melt rate for the dataset of Jenkins for the plume model; for the plume, box, linear and quadratic melting laws; for the estimations of Rignot et al.(2014) and Bernales et al. (2016)	57
5.3	Shelf profiles for stepwise increase of ocean temperature.	60
5.4	Grounding line retreat as a function of temperature	61
5.5	Grounding line retreat as a function of the mean melt over the first two thirds of the shelf	61
5.6	Maximum melt rate as a function of ocean temperature. Symbols as in Figure 5.4, but not filled.	63
6.1	Depth of shelf base and slope for the 12 independant shelves available in the dataset of A. Jenkins	68
6.2	Depth of shelf base and slope for the 12 independant shelves available in the dataset of A. Jenkins (Part 2)	69
6.3	Profiles of different shelf in depth-slope space.	71

6.4	Melting rates applies to the Jenkins dataset (plume model, box (un)tuned and plume parametrisations	72
6.5	Melting rates applies to the Jenkins dataset (plume (un)saturated, linear and quadratic melting laws	73
6.6	Steady-state sheet-shelf profile and slope values for the three numerical schemes tested (see text)	74
6.7	Sensitivity of maximum melt rate to changes in local slope for a logarithmic saturation	75
6.8	Sensitivity of mean sub-shelf melt rates to the maximum number of boxes of PICO. (Reese et al. (2018a), Supplementary Information	75
6.9	Grounding line migration due to varying maximum number of boxes n_{max} in the box parametrization.	76
6.10	Shelf profiles for stepwise increase of ocean temperature for the plume parametrization (see section 5.2).	76

List of Tables

2.1	Constant parameters used by the Lazeroms parametrisation	22
2.2	Matching the parameters that differ in the box and plume parametrisations . . .	28
5.1	Value of the parameters used for the grounding line retreat experiment.	59
6.1	The 12 transects used in the model comparison and temperature, salinity and grounding line depth	67
6.2	Mean melt rates (m/yr) from the different models considered	70

Chapter 1

Introduction and state of the art

Large portions of the Antarctic ice sheet are grounded below sea-level. Most of the coastal areas are comprised of ice shelves, wide bodies of flat floating ice that detach from the sea floor at the so-called grounding line. Most of the Antarctic mass balance is evacuated by these frontier regions where ice is in contact with the ocean. Iceberg calving and, mainly, basal melting below the shelves are the two major sinks of ice in the mass balance of the shelves that control outflow from the continent. Therefore, subshelf melting is the largest cause of mass loss from the sheet.

Subshelf melting is enhanced by the ice pump mechanism. Melting at depth releases buoyant freshwater at the ice-ocean interface. This water mixes with ambient ocean on its path towards the surface, accumulating even more freshwater. This leads to the formation of a growing plume, an upper layer of a stratified subshelf cavity that rises to the surface. Eventually, the plume may refreeze at low pressure, rejecting brine water that sinks and replenishes the cavity. Also, winter formation of sea ice can produce dense and cold saline water. These two mechanisms provide the cavity with cold and saline water in a thermohaline overturning circulation.

The ice shelves exert an important control on ice delivery to the ocean, and, thus, on the mass budget of the Antarctic ice sheet. Because of lateral shearing against the rocky shelf margins, and, occasionally, friction against seafloor hills at pinning points, the flux of ice is limited at the shelf sides and base. Transmission of stress slows down the ice flux upstream. This is called buttressing. Through buttressing, ice shelves limit the ice flux crossing the grounding line, and thus impede loss of grounded ice.

In case of reduced buttressing, as would be caused by shelf thinning, the buttressing effect

diminishes. The increased flux of ungrounded ice furnishes water to the ocean, leading to sea level rise. Of all freshwater containers, the Antarctic ice sheet has the largest potential of sea level rise. As the grounded ice accelerates and thins near the grounding line, it ends up reaching floatation. Grounding line retreat is thus a consequence of increased subshelf melting.

Particularly importantly, some ice streams around Antarctica have been reported to lie on a downsloping bedrock landward. When grounding line retreats, ice at the incremented grounding line gets thicker - thus, ice flow is larger, empowering loss of grounded ice and shrinking of the sheet. At the same time, freezing temperature lowers because of depth and melting rates inflate. As a consequence, a small perturbation of the grounding line unstabilizes the stream in a self-sustaining and irrevocable retreat: this is Marine Ice Sheet Instability.

The mass balance of Antarctica has been perturbed for the last decades because of global warming. If snowfall has become more important, boosting ice accumulation, it is not clear whether it compensates the rise in ablation processes. Climate projections forecast that polar air temperatures will rise by a few degrees within the next century. This will be accompanied by warming of the ocean waters in contact with the shelf base and changes in the water mass involved. In this context, assessment of future sea level rise needs to understand and evaluate properly the loss of buttressing from the tormented ice shelves.

Plethora of numerical models have been conceived for this purpose with varying precision and approximations. Some focus on reproducing estimated melting rates below real shelves while unravelling and implementing the relevant physics. These calculations are time-expensive and are usually applied only to single local shelves. Others try to simplify the calculation as much as possible in order to optimise computational speed without losing the key processes. This approach is ultimately aimed at application to full-scale coupling of sheet-shelf-ocean models for climate projections.

In this thesis, I focus on two parametrisations of two existing models describing subshelf melting: an explicit plume model (Jenkins, 1991) and its parametrisation of Lazeroms et al., (2018) on one hand; on the other hand, the parametrisation of Reese et al. (2018a) based upon the box model of Olbers and Hellmer (2010). They are compared and applied to a one-dimensional ice flow model to evaluate grounding line migration.

There are two aims of this thesis:

- compare the plume model, its parametrisation, and the box parametrisation, evaluate their agreement and compare them to simple parametrisations and retrievals from ice mass conservation;
- apply basal melting from these models onto a coupled ice sheet-shelf model and examine the evolution of the system.

For the first time, the plume parametrisation is coupled to an ice flow model and retroaction between shelf thinning and melt rates can be evaluated. The box parametrisation, on the other side, has already been coupled to two-dimensional ice flow models in the original paper, but here it will be readily compared to the plume parametrisation.

This document is structured as follows.

First, the thermohaline circulation by which subshelf melting is enhanced is described. The modifications triggered by human-induced global change are briefly cited and a short review of the literature on 1D subshelf melting and buttressing is proposed.

The second chapter describes the models that will be used in this thesis. The ice stream model is a flowline eulerian model, using the Shallow-shelf approximation, to which is coupled subshelf melting. The latter is included by implementation of, namely the plume model developed by Jenkins (1991); building on it, the plume parametrisation of Lazeroms et al. (2018); PICO, the box parametrisation of Reese et al. (2018a); linear and quadratic melting laws, respectively used in Beckmann and Goosse (2003) and Pollard and DeConto (2012).

The third chapter explores sensitivity to these melting models to changes in parameters and cavity properties. Water temperature, depth and depth gradient are the main control variables. The influence of salinity is bypassed by the use of temperature difference to surface freezing point.

The fourth chapter focuses on the coupling of the ice flow model to basal melting, raises caveats, approximations and limitations of the models. The plume parametrisation needs many adjustments to work correctly in the coupled set-up used in this thesis.

Finally, the fifth chapter compares the melt models with each other. They are shown to differ importantly. In a second part, the effect of subshelf melting to grounded ice is evaluated in an ideal situation. Although the melt models are very different, existence of threshold in grounding line retreat is found for all models at different ocean temperature.

1.1 Subshelf melting

Mechanisms

The overturning mechanism in shelf cavities is based on a circulation of Ice Shelf Water from the grounding line to shelf front, then back down to the continental shelf, usually downsloping landward, that guides the dense water towards the grounding line. This mechanism needs an input of energy at depth, that is carried by water. There are three sources of energy into the cavity (Jacobs et al., 1992):

- mode 1* winter formation of sea ice in open ocean releases High Salinity Shelf Water (HSSW) at surface freezing point. Due to buoyancy, this water sinks and follows the continental shelf towards the grounding line. Due to dependence of the freezing point on pressure ($-0.761^{\circ}\text{C}/\text{km}$), ice is brought to melting point. This mode is prominent in cold cavities, mainly Ross, Filchner-Ronne and Amery ice shelves (Dinniman et al., 2016).
- mode 2* the intrusion of Lower Circumpolar Deep Water inside the shelf cavity brings warm water at 3°C above the pressure freezing point. This water mass comes from the North-Atlantic Deep Water that mixes with the Antarctic Circumpolar Current (ACC) (Carter et al., 2009; Orsi et al., 1995). This induces important melting. Mode 2 is dominant in the Amundsen sector and the Antarctic Peninsula. Troughs in the seafloor, higher pycnocline as well as proximity of the ACC to the coastline foster invasion of the shelf cavity by this deep water (Orsi et al., 1999; De Rydt et al., 2014; Turner et al., 2017). The magnitude of HSSW winter formation is also likely to exert an important control by lowering the pycnocline (Petty et al., 2013).
- mode 3* Antarctic Surface Water, that forms in winter the HSSW, is warmer during summer. If intruding beneath the shelf, this can lead to melt rates similar in magnitude to *mode 2*, but closer to the front. Dinniman et al. (2016) review it to be major for the smaller shelves of East Antarctica.

Only modes 1 and 2 bear heat to the grounding line, and thus feed the overturning circulation.

As the overburden pressure decreases towards the shelf front, freezing point increases. Combined with the freshening of the plume, water can be supercooled by a few hundredths of a degree (Jones and Wells, 2018) and then freeze again.

Two mechanisms are at stake. If formation of columnar ice building on the shelf base was considered, it is minor compared to the in situ freezing catalysed by seed crystals (Jenkins and Bombosch, 1995). Accretion and consolidation of frazil onto the shelf base can amount to 60 meters thick, as observed by borehole drilling (Oerter et al., 1992). Holland et al. (2009) show that the low viscosity of marine ice may buttress and have a stabilizing effect on ice shelves by preventing cracking. Marine ice density can reach 920kg/m^3 (Craven et al. 2009) with salinity below 0.01% (Oerter et al., 1992).

The dynamics is still poorly constrained, and refreezing might occur within a few kilometres, depending on conditions (Jones and Wells, 2018). However, its impact on the plume properties (density as ice crystals are buoyant, but efficiently expel salt) can exhaust the plume before reaching the shelf edge. Remaining salty water would then sink again and replenish the overturning circulation.

The constitutive equations of the buoyant plume at one dimensions are briefly described in section 2.2.1. In this thesis, *mode 3* is ignored, and *mode 1* and *mode 2* are treated similarly as the deep ocean layers are not modelled. Modes *1* and *2* are only expressed through the choice of the far-field ocean temperature and salinity that serve as input for melt near the grounding line.

Climate change is not likely to warm the HSSW, as this water is at surface freezing point. The mixture of waters reaching the underside of the shelves, because of a tightening of the CDW (accompanied by a warming of the CDW) (Fyfe and Saenko, 2005; Hatterman and Levermann, 2010) and changes in the atmospheric forcing (Thoma et al., 2008), are most likely to evolve.

1.2 Marine Ice Sheet Instability

The Marine Ice Sheet Instability has been proposed 40 years ago (Weertmann, 1974; Thomas, 1979). The question is to know whether ice sheets grounded below sea level on landward downsloping bedrocks are stable. As ice flux across the grounding line increases with ice thickness, the deeper the grounding line, the larger the grounded ice discharge. A small perturbation from a steady state on a downsloping bedrock would henceforth trigger a dramatic grounding line retreat. Though the absence of neutral equilibrium on downloping bed has been contradicted (Hindmarsh, 1993) or tempered (Hindmarsh, 2006), it has since be supported (Schoof, 2007a). It is also demonstrated that some requirements in precision to model grounding line migration

were not fulfilled in the rebuttals (Viel and Payne, 2005; Pattyn, 2006).

These models either ignored buttressing, either used a simplified second horizontal dimension. Taking explicitly an independent second horizontal dimension, Gudmundsson et al. (2012) and Gudmundsson (2013) show that buttressing can put an end to MISI.

However, none of these models do take into account physically-derived subshelf melting. I expect that the lowering of the freezing point with depth should increase melt as the grounding line retreats, thus accentuating the MISI. This would need confirmation by 3D oceanic models to evaluate the mixture and circulation of water mass that reaches the deeper grounding lines. If basal melt positive feedback has to my knowledge not been identified as a key mechanism in MISI, it has the capability to trigger it (Hillebrand et al., 2017; Jenkins et al., 2018)

Either way, some ice streams in West Antarctica might already have entered a period of collapse involving MISI (Favier et al., 2014; Joughin et al., 2014), which are likely to lead to disintegration of substantial part of the West Antarctic ice sheet (Rignot et al., 2014) as much of it is grounded deeper than the enclosing grounding lines (Pollard et al., 2015).

1.3 Ice-ocean coupling with buttressing

Ice shelf buttressing is due to lateral drag of an ice mass against the walls of the stream. Lateral drag and longitudinal stress exerts the largest control on ice flow near the grounding line where basal drag becomes negligible (Viel and Payne, 2003).

Parizek et Walker (2010) implement an adapted version of the plume model of Jenkins (1991) into an ice stream model grounded below sea level with two horizontal dimensions. Domain is laterally confined between walls 40km distant from each other to account for buttressing. They show that the dynamics of grounding line retreat depends on the initial conditions, when applying melting onto not stable systems. As Walker and Holland (2007), they find a positive melt-slope feedback, meaning that increasing slopes dopes the plume velocity, hence turbulences and melting, accentuating the slope.

Applying arbitrary melting rates, Walker et al. (2008) show that the grounding line migration is most sensitive to melting near the grounding line.

Chapter 2

Models: Description

This section describes the models used in this thesis. Ice flow is calculated via a typical Shallow-Shelf Approximation using common parametrisation of shelf front and buttressing. The plume and box parametrisations are developed in their original papers, and the main equations are summarized here for clarity. The plume model is much more common, as well as the two depth-dependant parametrisations that are used in large-scale modelisation.

2.1 SSA ice flow model

The ice flow model is a vertically-integrated coupled sheet-shelf model using the shallow-shelf approximation¹ (MacAyeal, 1989) on a fixed grid. These models have been recognised (Pattyn et al., 2012; Pattyn et al., 2013) to guarantee the capture of grounding line motion through transmission of membrane stress.

Velocity of ice is calculated with the same formulation for both sheet and shelf, according to the force balance in Rommelaere and Ritz (1996):

$$\frac{\partial}{\partial x} \left(\eta h \frac{\partial u}{\partial x} \right) + \frac{\partial h \tau_{xy}}{\partial y} - \tau_b = \tau_d \quad (2.1)$$

¹A L1L1* (Hindmarsh, 2004) hybrid version using SIA for the sheet plus SSA for the entire domain (as in Winkelmann et al., 2011) showed less stable and was not used. Precision on grounded mass lost is thus sacrificed (Pattyn et al., 2013).

The driving stress τ_d is the along-slope component of the ice shear stress induced by the height gradient of the ice column. It is function of height and surface slope only:

$$\tau_d = \rho_i g h \frac{\partial s}{\partial x}$$

The effective viscosity η is a function of temperature and strain rate because ice is a visco-plastic body:

$$\eta = \frac{1}{2} A^{-1/n} \left| \frac{\partial u}{\partial x} \right|^{\frac{1-n}{n}} \quad (2.2)$$

The vertically-integrated viscosity parameter A will be examined in the next section. It is homogeneous and taken constant for each experiments throughout the shelf. Above grounded ice, the basal shear stress τ_b is velocity-dependant (Weertman, 1974):

$$\tau_b = \beta^2 = u_b^{m-1} c^{-m} \quad (2.3)$$

where c and m are constants, and it is zero below the shelves. This assumes a transition zone narrower than grid size, which is expected to increase sensitivity to melt rate (Pattyn et al., 2006). However, is is likely to exacerbate the need for a high resolution, as show Gladstone et al. (2017).

Lateral drag is parametrised according to Van der Veen and Whillans (1996), as in Vieli and Payne (2003). Buttressing is due to lateral shearing against the walls of the stream. In this case, assuming constant width $2W$ along the stream, constant ice thickness throughout the width and grounding line position (that allows for a uniformly distributed lateral drag), and no slip at the margins, lateral drag can be implemented in the left-hand term of eq. (2.1) in the form of:

$$\frac{\partial h \tau_{xy}}{\partial y} = \frac{h}{W} \left(\frac{n+2}{2AW} \bar{u} \right)^{1/n} \quad (2.4)$$

where \bar{u} is the width-averaged velocity. The equation (2.1) thus contains a buttressing term that restrains the ice from flowing freely. This traction linearly depends on ice thickness. Thus, the thinner the shelf (or the sheet), the lower the buttressing effect and the faster the flow.

The velocity field is calculated on a staggered grid using a semi-implicit numerical scheme, that allows for relatively large time-stepping (equivalently to better stability) (Press et al., 1992).

The mass balance is then given by the continuity relation:

$$\frac{\partial h}{\partial t} = \dot{m}_b - \frac{\partial}{\partial x} (uh) \quad (2.5)$$

with the mass balance comprised of surface mass balance \dot{a} and basal mass balance, \dot{m} , on which focuses this thesis. As for velocity, a semi-implicit numerical scheme is used.

Boundary conditions for solving the differential equations still need to be defined. At the ice divide, a Neumann boundary condition is imposed on ice thickness $\frac{\partial h}{\partial x} = 0$ and flux at the first gridpoint on the left part of the ice divide equals, with the opposite sign, flux towards the right. This states that the ice sheet is symmetric around the ice divide. A calving front is parametrised at the end of the domain, using the force balance at floatation, according to MacAyeal (1989):

$$\int_{\frac{\rho_i}{\rho_w} h}^{\left(1 - \frac{\rho_i}{\rho_w}\right)h} \sigma \cdot \vec{n} = -\frac{1}{2} g \rho_w \left(\frac{\rho_i}{\rho_w} h \right)^2 \vec{n} \quad (2.6)$$

To avoid numerical errors, a lower limit for ice thickness is prescribed : $\min(h) = 10^{-5}\text{m}$. This is thin enough to exert no buttressing on ice upstream.

2.2 Basal melt models

Common hypothesis are made in the plume model and the plume and box parametrisation. Mainly, they assume a steady-state under the rationale that ocean dynamics evolve much faster than the ice, and can thus equilibrate within the time scales of ice deformation. This is a questionable assumption, as the influence of tides is prominent both for water velocity and melting. This was shown in cold cavities (Makinson et al., 2011; Arzeno et al., 2014) where the ice pump mechanism is in principle relatively less efficient, but this also strongly depends upon geographic factors (Dinniman et al., 2016). At 0.1m/s for a 10km long shelf, it takes more than one day for melt water from the grounding line to reach the front; it would have undergone a few tides. The steady-state could then be interpreted as time-averaged, including parametrisation of tides in, for example, the exchange coefficient that are still poorly constrained (Dinniman et al., 2016).

Also, they ignore the velocity-related drop predicted by the Bernoulli equation:

$$\frac{1}{2} v^2 \rho_w + g z_b \rho_w + p = Cst.$$

This is justified by the order of magnitude of each term: $\frac{1}{2} \times 0.1^2 \times 1000 + 10 \times 100 \times 1000 + 10 \times 101300 \approx 10^1 + 10^6 + 10^6 = Cst$.

They all ignore the typical effects emerging with the second horizontal dimension. This is the case of shelf base geometry and the Coriolis effect. Together, they determine the plume water path and areas where water may accumulate (Holland et al., 2007; Holland and Feltham, 2006). Although flowline models should technically reproduce the same melt patterns if given

the appropriate transect, they become obsolete when integrated in a non-steady coupled model. Basal melting is indeed likely to induce changes in geometry that would impact the flowline. As such, these 1D models are only indicative.

2.2.1 Plume model

The plume model is presented in Jenkins (1991). Here are only summarized the main equations used in the MatLab code, that may differ slightly from the ones described in the original paper. Notations are inspired by Lazeroms et al. (2018). The Coriolis effect is ignored in one dimension.

This model involves explicitly the subshelf overturning circulation mechanism. Fresh melt-water at depth, whilst mixing with ambient saline water, forms a buoyant plume. Further melting, friction, and mixing affect velocity, mass, temperature and salinity of the rising plume across its path to the shelf front. Buoyancy is calculated against temperature-salinity vertical profile, such that the ocean stratification is taken into account.

The model is thus comprised of four vertically-integrated differential equations for mass, momentum, heat and salt conservation. Variables are the thickness of the plume D , temperature T , velocity U and salinity S and evolve along the plume path:

$$\begin{aligned}
 \frac{dDU}{dX} &= E_0 U \sin \alpha + \dot{m} \\
 \frac{dDU^2}{dX} &= D \frac{\Delta \rho}{\rho_0} g \sin \alpha - C_d U^2 \\
 \frac{dDUT}{dX} &= E_0 U \sin \alpha T_a + \dot{m} T_b - \sqrt{C_d} \Gamma_T U (T - T_b) \\
 \frac{dDUS}{dX} &= E_0 U \sin \alpha S_a + \dot{m} S_b - \sqrt{C_d} \Gamma_S U (S - S_b)
 \end{aligned} \tag{2.7}$$

where α is the slope of the shelf base and g is the gravity constant. E_0 , C_d and $\sqrt{C_d} \Gamma_T$ are given in Table 2.1. $\sqrt{C_d} \Gamma_S$ and $\sqrt{C_d} \Gamma_T$ are Stanton numbers that relate to a linear dependency on velocity of the turbulent exchange. This dependence was identified by Kader and Yaglom (1973) under the hypothesis of a fully turbulent flow. As acknowledged by Jenkins et al. (2010), this implicitly assumes that the shelf base is almost perfectly even².

Four sets of temperature and salinity are relevant:

²For plume velocity of $\approx 0.1\text{m/s}$ at 0°C , the size of bumps must be larger than 10cm to enter the turbulent regime, as calculated by the Reynolds number: $Re = \frac{\rho u L}{\mu} \Rightarrow L \approx \frac{4000 \times 1.79 \times 10^{-3}}{10^{-3} \times 0.1} \approx 0.072\text{m}$

- the bulk of ice : (T_i, S_i) , where $S_i \approx 0$ even in case of refreezing
- the boundary layer, a thin interface between the ice and the plume, where the melting and freezing physics takes place: (T_b, S_b)
- the supposedly well-mixed plume: (T, S)
- the conditions of the ambient water below the plume : (T_a, S_a)

The thermodynamics of the the boundary layer is detailed in Holland and Jenkins (1999). Heat divergence in the boundary layer, resulting from diffusion in ice and turbulent heat exchange in liquid water, is compensated by phase change. Salinity of the boundary layer mixes with the plume. Melting rate can be linked to water salinity and temperature through:

$$\begin{aligned}\sqrt{C_d}\Gamma_S U (S - S_b) &= \dot{m} S_b \\ \sqrt{C_d}\Gamma_T U (T - T_b) &= \dot{m} \frac{L}{c_w} + \frac{c_i}{c_w} (T_b - T_i)\end{aligned}\tag{2.8}$$

with L , c_i and c_w the usual latent heat of fusion and heat capacities respectively of ice and water. In case of refreezing, inclusion of salt in the ice lattice is neglected. The freezing point condition at the ice-water interface (see Table 2.1 for the coefficients) is:

$$T_b = \lambda_1 S_b + \lambda_2 + \lambda_3 z_b\tag{2.9}$$

The driving force is buoyancy of the plume, which is a function of density:

$$\frac{\rho_a - \rho}{\rho_0} = \beta_S(S_a - S) - \beta_T(T_a - T)\tag{2.10}$$

This equation is discussed in section 2.2.3.

2.2.2 Plume parametrization

Based on the work of Jenkins (2011), Lazeroms et al. (2018) elaborate a 1D parametrization of the plume model (Jenkins 1991) in order to optimize computational speed. Approximations are used to represent mechanisms of mixing, heat and salt exchange, that are water velocity-related and depend on shelf base geometry. In particular, the ocean is supposed to be unstratified (i.e. with homogeneous salinity and temperature). Melting is induced by the action of an effective temperature (see Lazeroms et al. 2018, Fig. 7b).

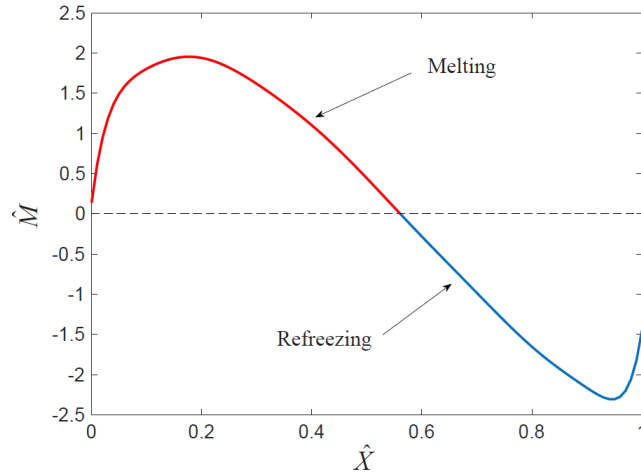


Figure 2.1: Dimensionless melt curve $\hat{M}(\hat{X})$ used in the basal melt parametrization described in Lazeroms et al. 2018.

In this parametrisation, it is assumed that all plumes undergo the same physics, adjusted only by local peculiarities. Thus, they can all be characterised by the use of a dimensionless depth ranging from 0 to a maximum of 1, that comprehends the evolution of the plume. This includes largest melting in the vicinity of the grounding line to possible refreezing downstream if the conditions (temperature, pressure, salinity) allow it (see Figure 2.1). This dimensionless depth serves as the spatial coordinate. Melting rate is then a function of this spatial coordinate, scaled up in regard to local slope, depth, temperature and salinity.

This section summarizes the calculation of the dimensionless coordinate \hat{X} and the melt rate \dot{m} as described in Lazeroms et al. (2018).

Dimensionless spatial coordinate

The 1D dimensionless spatial coordinate \hat{X} , standing for depth, is defined as (eq. A11 in the original paper):

$$\hat{X} = \frac{z_b - z_{gl}}{l} \quad (2.11)$$

z_b is the local depth of the shelf base (assuming the floatation condition $|z_b|\rho_w = h\rho_i$), z_{gl} is the depth of the grounding line, while l contains the typical length scale associated with temperature difference with freezing point at the grounding line, adapted with a slope-dependant geometrical

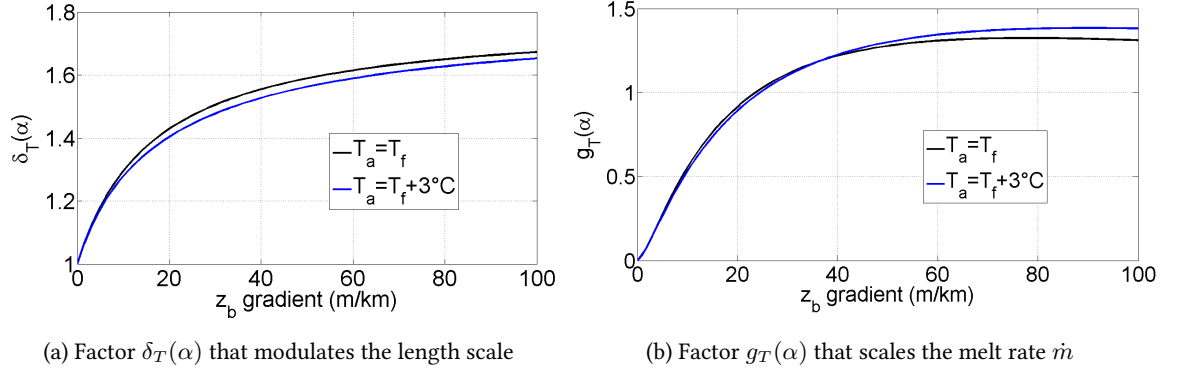


Figure 2.2: Sensitivity to slope. Sensitivity is largest below 30m/km where most of the ice shelves lie. Largest slopes encountered throughout the dataset of the plume model (A. Jenkins) range 200m/km (with $\Delta x = 500\text{m}$), largest mean slope from grounding line to shelf front is 42.4m/km. Some examples are given in Figure 6.3.

factor shown at Figure 2.2 (eq. A10):

$$l = \frac{T_a - T_{f,gl}}{\lambda_3} \delta_T(\alpha)$$

T_a and $T_{f,gl}$ are respectively ambient ocean temperature and grounding line freezing point. λ_3 is the dependence of freezing point on depth in eq. (2.9). Values of the constants are given in Table 2.1. In the slope dependant factor $\delta_T(\alpha)$ lie E_0 a coefficient relating slope to entrainment rate, α the slope and x_0 an empirically determined coefficient:

$$\delta_T(\alpha) = \frac{x_0 \sqrt{C_d} \Gamma_{TS} + E_0 \sin \alpha}{x_0 (\sqrt{C_d} \Gamma_{TS} + E_0 \sin \alpha)}$$

The turbulent exchange coefficients for heat and salt, namely Γ_T and Γ_S in the plume model, are here simplified into one unique effective turbulent exchange coefficient Γ_{TS} . Γ_{TS} itself contains local slope and local temperature dependences (eq. A8)³:

$$\Gamma_{TS} = \Gamma_T \left(\gamma_1 + \gamma_2 \frac{T_a - T_f}{\lambda_3} \frac{E_0 \sin \alpha}{\sqrt{C_d} \Gamma_{TS_0} + E_0 \sin \alpha} \right)$$

where Γ_T , γ_1 , γ_2 and Γ_{TS_0} are given in Table 2.1. Imposing the ice-ocean boundary at pressure freezing point (eq. 2.9) and writing $\gamma_{TS} = \sqrt{C_d} \Gamma_T U$, eq.(2.8) is simplified:

$$\gamma_{TS} (T - T_f) = \dot{m} \frac{L}{c_w} + \frac{c_i}{c_w} (T_f - T_i) \quad (2.12)$$

³With a correction to the temperature-dependant term. Turbulent exchange indeed depends on local properties and $T_{f,gl}$ should therefore be replaced by T_f .

Constant parameters	Symbol	Values	Units
Entrainment rate	E_0	3.6×10^{-2}	
Freezing point-salinity coefficient	λ_1	-5.73×10^{-2}	$^{\circ}\text{C}/\text{psu}$
Freezing point offset	λ_2	-8.32×10^{-2}	$^{\circ}\text{C}$
Freezing point-depth coefficient	λ_3	-7.61×10^{-4}	$^{\circ}\text{C}/\text{m}$
Drag coefficient	C_d	2.5×10^{-2}	
Turbulent heat exchange coefficient	$\sqrt{C_d}\Gamma_T$	1.1×10^{-3}	
Heat exchange parameter	$\sqrt{C_d}\Gamma_{TS_0}$	6.0×10^{-4}	
Scaling factor	x_0	0.56	
Heat exchange parameter	γ_1	0.545	
Heat exchange parameter	γ_2	3.5×10^{-5}	$./\text{m}$

Table 2.1: Constant parameters used by the Lazeroms parametrisation

\hat{X} ranges from 0 at the grounding line to 1 when the plume has lost all its momentum due to refreezing, friction and too small buoyancy (Jenkins 2011). This means that $\hat{X} = 1$ is not the shelf front but the furthest point the plume can reach; further melt is not described by the model. However, in practice, this should virtually never happen. Indeed, assuming a nil basal slope, it holds:

$$1 = \frac{z_b - z_{gl}}{T_a - T_{f,gl}} \lambda_3$$

For constant ocean salinity and temperature (hypothesis needed for this parametrization), the pressure freezing point at the grounding line can be rewritten, and eventually we find:

$$T_a = \lambda_1 S_a + \lambda_2 + \lambda_3 z_b$$

which means that for reaching $\hat{X} = 1$, the shelf base must be shallow enough so that ocean water (not the plume freshwater) freezes, which can only occur near surface. Henceforth, the shelf front is met for $\hat{X} \leq 1$. In the following, $T_a \geq T_f^{surf}$ is considered.

Figure 2.3 illustrates the dimensionless coordinate \hat{X} along the Filchner-Ronne Ice Shelf.

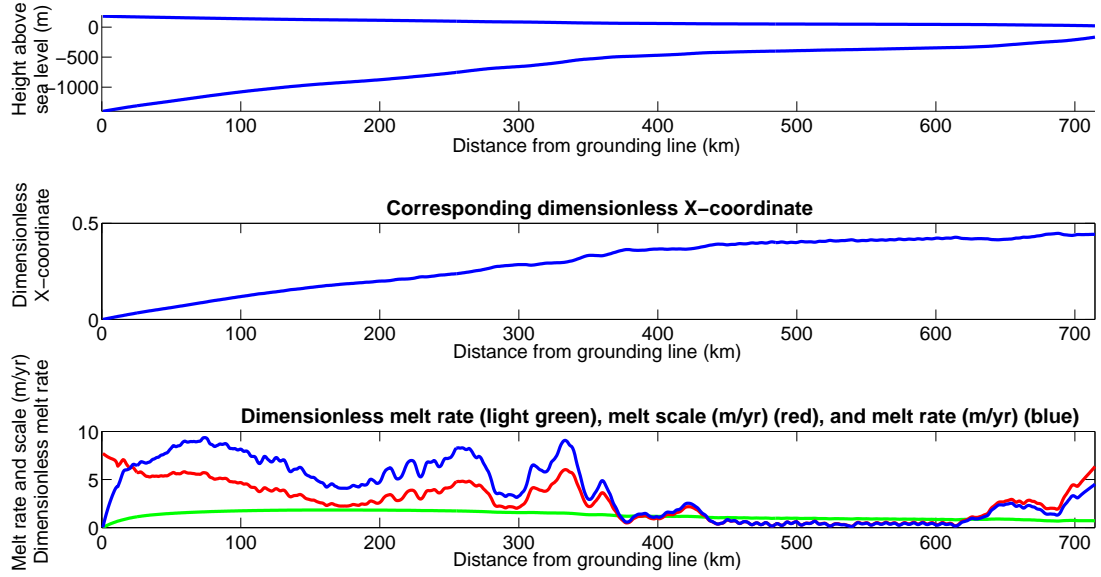


Figure 2.3: Relation between basal depth, dimensionless variables and melt rate. The transect is the taken from Lazeroms et al. (2018), Fig.5a. $T_a = T_f^{surf} + 0.8^\circ\text{C} = -1.1^\circ\text{C}$.

Melt rate

Melt rate is calculated as the product of a temperature and geometry dependant melt scale times a dimensionless melt curve derived from Jenkins 2014 applied to the horizontal distance. Thus, melt rate is (eq. A12)⁴

$$\dot{m} = M \times \hat{M}(\hat{X})$$

where M depends quadratically on temperature, and through a geometrical factor on slope (eq. A9):

$$M = 10g(\alpha) (T_a - T_{f,gl})^2 \quad (2.13)$$

and \hat{M} is a 11-th order polynomial function of \hat{X} (eq. A13), represented at Figure (2.1). The coefficients of the polynom represented in this figure have values differing from those given in the paper. The real values of these coefficients were obtained directly from W. Lazeroms (personal communication) thanks to H. Goelzer participation. However, before accessing them, an algorithm-decoding image was developed that could be applied to (2.1) as a .tif file to fit a 11-th order polynom.

⁴This expression is an input of meltwater into the plume and thus does not exactly measures the ice thickness change.

Images are RGB matrices with values ranging between 0 (black) and 255 (white) for the three color components. This allows for detection of grey and coloured pixels with arbitrary precision. After rescaling (using the darkest integrated columns and lines for the axes), the curve can be easily fitted. Only the published values differ significantly from the communicated ones.

The code is validated against the results obtained by Lazeroms et al. 2018 for one-dimensional shelf profiles (their Figure 5). The shelf depth is retrieved using the same kind of image treatment as above. As expected, they match exactly.

Retrieval of horizontal distance and associate melt rate is straight-forwardly performed using:

$$\dot{m} = M_i \hat{M}(\hat{X}_i) = M(z_i; T_a, T_{f,gl}, \alpha_i) \hat{M}(\hat{X}(z_i; T_a, T_{f,gl}, \alpha_i))$$

Final melt pattern and rate thus depend on the shelf geometry, ambient ocean properties, and on the path along the universal melt curve shown at Figure (2.1), which depends on the dimensionless position \hat{X} . Shelf profile, dimensionless melt, melt scale and melt rate are shown at Figure 2.3 for the Filchner-Ronne ice shelf transect. Sensitivity of \hat{X} and \dot{m} are examined in the next section.

2.2.3 Box parametrization (PICO)

The box parametrization (Reese et al. 2018a) is a simplification of the box model developed by Olbers et Helmer (2010). Here, the plume evolution is not locally evaluated at each gridpoint along its path. Instead, properties of the plume are advected across a certain number of boxes of area A_k , temperature T_k , salinity S_k , experiencing melt rate \dot{m}_k within which they are locally adjusted. Assuming a steady-state, advection of temperature and salinity is given by :

$$\begin{aligned} q(T_{k-1} - T_k) + A_k(\dot{m}_k + \gamma_T)(T_{bk} - T_k) &= 0 \\ q(S_{k-1} - S_k) + A_k(\dot{m}_k + \gamma_S)(S_{bk} - S_k) &= 0 \end{aligned} \tag{2.14}$$

There is advection from box $k-1$ to box k and from the meltwater originating from the boundary layer into the plume. To this advection is added a turbulent exchange term between the boundary layer and the plume.

Water flux below the shelf is parametrized by the overturning coefficient C as a function of density:

$$q = C(\rho_0 - \rho_1) \tag{2.15}$$

where ρ_0 is the density of the ocean and ρ_1 of the first box. This way, large-scale buoyancy effectively determines the overturning strength. Within each box, melting or refreezing, dependant on the effective turbulent exchange coefficient γ_T^* (detailed in section 2.2.3), locally depends on temperature difference to pressure freezing point (eq. 2.9) through:

$$\dot{m}_k(x) = -\frac{\gamma_T^* c_w}{\nu L} (T_{f,k} - T_k(x)) \quad (2.16)$$

with $\nu = \frac{\rho_i}{\rho_w}$, L latent heat of fusion in J/Kg and p_k the overburden pressure. Here, the second dimension y is already implicit as it will not be used in the flowline models.

Temperature and salinity of the box $k - 1$ are averaged over their box and used as boundary conditions to find $T_k(x)$ and $S_k(x)$. In the first box, one should solve for overturning flux q , T_1 , S_1 and \dot{m}_1 . Temperature is given by:

$$T_1(x) = T_a + \frac{\vartheta(x)}{2} - \sqrt{\frac{\vartheta(x)^2}{2} - \vartheta(x) (T_f^{gl} - T_a)}$$

with T_f^{gl} the pressure freezing point at the grounding line and $\vartheta(x) = \frac{A_1 \gamma_T^*}{C \rho^* (\beta \frac{S_a c_w}{\nu L} - \alpha)}$. Salinity then reads

$$S_1 = S_a \left(1 + c_w \frac{T_1 - T_a}{\nu L} \right)$$

from which density can be obtained through:

$$\rho = \rho_* [1 - \alpha (T - T_*) + \beta (S - S_*)] \quad (2.17)$$

ρ^* is a reference density discussed in section 2.2.3, as well as the coefficients α and β ; $T_* = 0^\circ\text{C}$ and $S_* = 34\text{psu}$. Overturning flux q is calculated according to (2.15) and local melt rate $\dot{m}_1(x)$.

For box k , temperature is given by

$$T_k = T_{k-1} + \frac{A_k \gamma_T^* (T_f^{k-1} - T_{k-1})}{q + A_k \gamma_T^* - \frac{A_k \gamma_T^* c_w}{\nu L} a S_{k-1}}$$

As stated above, quantities from box $k - 1$ that are advected into box k are averaged over box $k - 1$. The continuous expression would be

$$Q_{k-1} = \frac{1}{A_{k-1}} \int_a^b Q_{k-1}(x) dx$$

a and b being the borders of box $k - 1$.

The number of boxes is given by:

$$n = 1 + rd \left(\sqrt{d/d_{max}} (n_{max} - 1) \right) \quad (2.18)$$

where rd is a rounds to the nearest integer, d is the length of the shelf, $d_{max} = 650\text{km}$ and $n_{max} = 5$ is a model parameter which will be examined in section 4.2. Boxes are then affected to grid cells such that they all have the same surface A_k , assuming a semi-circular shelf.

This model ignores basal slope, velocity-dependant turbulences, and the Coriolis effect.

Code

The code was provided by F. Pattyn as a 1D version of the parametrisation described in Reese et al. (2008a). It differs to the one described in the original paper in that the overturning flux is calculated separately for each box, i.e. $q_k = C(\rho_0 - \rho_k)$ and not once and for all with the first box. However, this changes virtually nothing to the result.

The model being conceived for two dimensions, an appropriate treatment of the loss of this second dimension to the flowline model must be developed. Two different ways are compared: either using semi-circular shelf, corresponding to the governing idea of the original paper, either using a rectangular shelf to match the set-up of the coupled sheet-shelf-ocean experiments with the parametrised buttressing factor W (see section 2.1). Changes of the shape of the basin on the mean melt rate and mean melt rate over the first box are shown in Figure 2.4. There is little difference between the two models. Practically, the rectangular basin yields boxes of constant length, while the first boxes of the semi-circular basin are shorter. Melt is thus less concentrated in the rectangular configuration.

Moreover, the overturning coefficient C is parametrised in Reese et al. (2018a) considering a specific geometry. As the geometry changes, a new criterion should be formulated to better constrain C in the rectangular case. The chosen criterion is the value of C providing the best adequacy with the plume parametrisation. If the two parametrisations can be tuned to yield similar melt rates, then the behaviour of the coupling to an ice stream model can be compared. This tuning is even more indicated as some constants will be changed (see next section, Table 2.2).

Matching the parameters of the two parametrisations

In order to produce a meaningful comparison of the physical features of both models, the parameters used are matched. Therefore, remaining discrepancies in the results will be the consequence

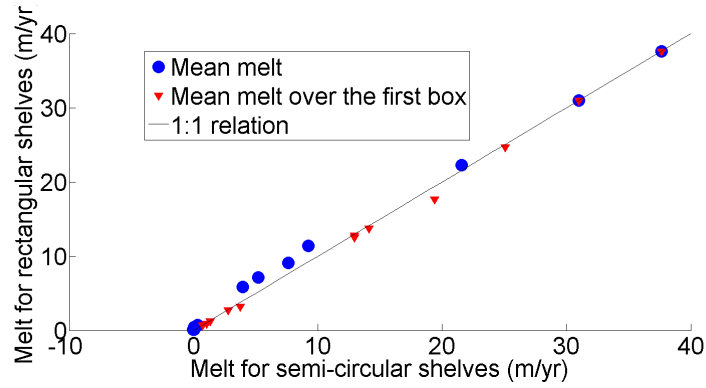


Figure 2.4: Comparison between mean melt over entire shelves and over first box for the 12 distinct selected shelves from the dataset of Jenkins (Table 6.1). Radius of semi-circular shelves is the total length given in the dataset. For rectangular shelves, width is chosen so that total area is the same ($A = LW = 1/2\pi L^2$).

of the approximations only.

In Table 2.2 are gathered the parameters used both in the plume and in the box parametrization. Comparison for some of those is rather straight-forward. Hereunder are developed those which require some calculation. The overturning coefficient C is absent from the plume parametrization.

As the plume parametrisation makes use of an "empirically derived dimensionless scaling factor" x_0 , whose value is not further justified, the parameters will all be set to the ones used in the paper of Lazeroms et al. (2018).

Density In the plume model and its parametrisation, water density is expressed in relative terms (eq. 2.10)

$$\frac{\rho_a - \rho}{\rho_0} = \beta_S(S_a - S) - \beta_T(T_a - T)$$

while Reese et al. (2018a) calculates (eq. 2.17):

$$\rho = \rho_* [1 - \alpha(T - T_*) + \beta(S - S_*)]$$

where ρ_0 is implicit as the entire fraction is implemented as a whole. Its value is only given in the MatLab code of the plume model by A. Jenkins. As only density contrasts are needed in the three models, we should then find adequacy between the values of Lazeroms et al. (2018) (L) and

Parameter	Equation	Lazeroms et al. (2018)	Reese et al. (2018a)
λ_1	(2.9)	$-0.0572 \text{ }^\circ\text{C/psu}$	$-0.0572 \text{ }^\circ\text{C/psu}$
λ_2	(2.9)	$0.082 \text{ }^\circ\text{C}$	$0.0788 \text{ }^\circ\text{C}$
λ_3	(2.9)	$7.61 \times 10^{-4} \text{ }^\circ\text{C/m}$	$7.84 \times 10^{-4} \text{ }^\circ\text{C/m}$
ρ_0, ρ_*	(2.10),(2.17)	1030 kg/m^3	1033 kg/m^3
β_T, α	(2.10),(2.17)	$3.87 \times 10^{-5} \text{ }^\circ\text{C}$	$7.5 \times 10^{-5} \text{ }^\circ\text{C}$
β_S, β	(2.10),(2.17)	$7.86 \times 10^{-4} \text{ psu}^{-1}$	$7.7 \times 10^{-4} \text{ psu}^{-1}$
γ_{TS}, γ_T^*	(2.12), (2.16)	$\sqrt{C_d} \Gamma_T U$	$2 \times 10^{-5} \text{ m/s}$
C	(2.15)	/	$10^6 \text{ m}^6 \text{ kg}^{-1} \text{ s}^{-1}$

Table 2.2: Matching the parameters that differ in the box and plume parametrisations

Reese et al. (2018a) (R):

$$\left(\frac{\rho_a - \rho}{\rho_0} \right)^L = \left(\frac{\rho_a - \rho}{\rho_0} \right)^R$$

Using the expression from eq. (2.17) for ρ_a and ρ , we find:

$$\beta_S (S_a - S) - \beta_T (T_a - T) = \frac{\rho_*}{\rho_0} [\alpha (T - T_a) - \beta (S - S_a)]$$

The easiest is thus to set:

$$\begin{cases} \beta = \beta_S \\ \alpha = \beta_T \\ \rho_* = \rho_0 \end{cases}$$

Effective turbulent exchange coefficient These coefficients represents the mixing between the boundary layer at the ice-ocean interface and the Ice Shelf Water below. In the plume model, a formulation of heat and salt exchange using respectively Γ_T and Γ_S is used. However, the two parametrisations use instead a simpler formulation, since McPhee (1992) demonstrates that heat and salt are predominantly exchanged altogether by the action of eddies. The plume and box parametrisations thus use effective exchange coefficients, respectively noted γ_{TS} (eq. 2.12) and γ_T^* (eq. 2.16). Neglecting the heat transfer through ice, melt rates in the simplified version of the plume model becomes:

$$\dot{m}_p = \frac{\gamma_{TS} c_w}{L} (T - T_f)$$

which looks like the expression of the box parametrisation:

$$\dot{m}_b = \frac{\gamma_T^* c_w}{\nu L} (T - T_f)$$

The factor $\nu = \frac{\rho_i}{\rho_w} \approx 0.89$ comes from the fact that \dot{m}_b measures the evolution of the thickness of ice and is thus expressed in meter of ice per year. Latent energy is exchanged with the water of the implicit plume in the right-hand term. The plume parametrisation, however, is explicitly based on the plume and melt rate \dot{m}_p is an input of meltwater (positive or negative) into the plume, as required by eq. (2.7). For the coupling to the ice stream model, a factor ν shall thus be included in the melt rate yielded by the plume parametrisation. This will not affect x_0 .

The effective turbulent exchange coefficient γ_{TS} depends linearly on speed in the parametrisation of the plume model: $\gamma_{TS} = \sqrt{C_d} \Gamma_T U$. The plume model yields speed between 0.02 and 0.1m/s for the Ronne Ice Shelf, and reaches 0.7m/s for the Pine Island Glacier and Jakobshavn Isbrae. γ_{TS} therefore ranges between 2×10^{-5} to 8×10^{-4} m/s. This is to be compared to the value of $\gamma_T^* = 2 \times 10^{-5}$ m/s chosen by Reese et al. (2018a) after an empirical tuning, throughout all ice shelves of Antarctica, satisfying:

- freezing must not occur in the first box;
- melt rate must decrease between the first two boxes (this recalls the melt pattern of the plume parametrisation, Figure 2.1);
- melt rates of Pine Island Glacier and Filchner-Ronne Ice Shelf should be close to the observations (respectively, warm and cold cavity).

This tuning is of relatively little meaning in this thesis, because the shape of the shelves is prescribed (rectangular) and some constants have been changed (Table 2.2). However, as the box parametrisation does not explicitly calculate the plume velocity, γ_T^* should remain constant and can not be assimilated to γ_{TS} . It could be related to the overturning flux q , but the thickness of the plume would be missing. For this reason, another tuning of γ_T^* is performed hereafter, seeking for the best match between the two parametrisations.

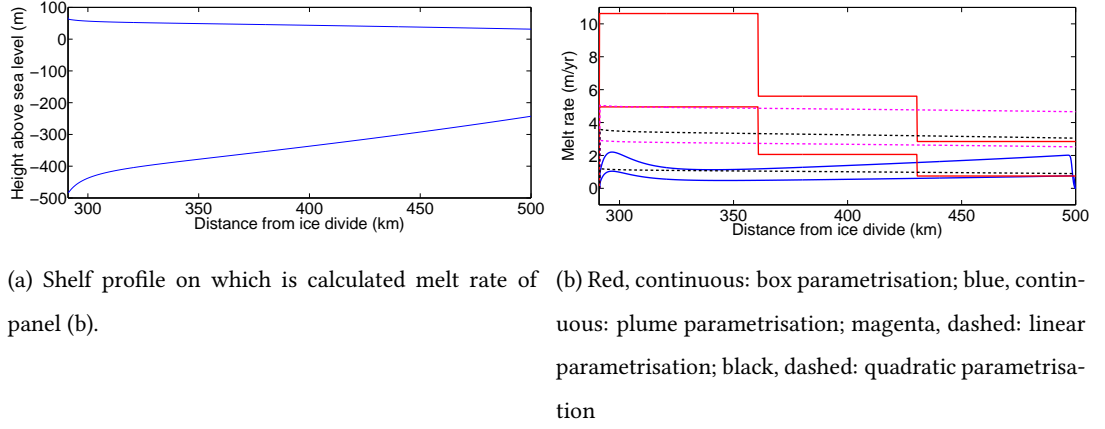


Figure 2.5: The four parametrizations used in this thesis for ocean temperature 1°C and 2°C above surface freezing point.

2.2.4 Depth-dependant parametrizations

Beckmann and Goosse (2003) suggest a melt rate linearly related to depth and temperature:

$$\dot{m} = \frac{\rho_w c_w \gamma_T}{\rho_i L_i} (T_a - T_f(z_b)) \quad (2.19)$$

where $c_w = 4000\text{J}/(\text{kg}^\circ\text{C})$ is the heat capacity of liquid water, $L_i = 334000\text{J}/\text{kg}$ is the latent heat of fusion, and γ_T is a tuning constant. Contrarily to Beckmann and Goosse (2003), melt rate is calculated locally, making T_f depending on basal depth (whereas the original equations only makes use of the depth of the shelf front). For $\gamma_T = 10^{-4}$, this yields melt rate of about 10m/yr at 500m deep with $T_a = T_f^{surf}$.

In accordance with Holland et al. (2008), DeConto and Pollard (2016) and Pollard and DeConto (2012) use a quadratic melting law, assuming that the effective turbulent heat coefficient γ_T also depends on temperature. Melt rate is thus given by:

$$\dot{m} = \frac{\rho_w c_w K_T}{\rho_i L_i} |T_a - T_f(z_b)| (T_a - T_f(z_b))$$

where K_T is a tuning constant (Martin et al., 2011).

γ_T and K_T are tuned so that they yield similar mean melt rates than the estimations of Rignot et al. (2013) and Berales et al. (2016) for the shelves of the dataset of A. Jenkins (see melt distribution in Figure A.6.5, mean melt rate in Table A.6.2). We use $\gamma_T = 5 \times 10^{-6}\text{m/s}$ and $K_T = 2 \times 10^6\text{m}/(\text{s}^\circ\text{C})$, respectively 1/20th and four times the original values.

The four parametrisations are compared in Figure 2.5 when applied on a modelled ice shelf.

Chapter 3

Models: Sensitivity analysis

3.1 SSA Ice flow model

In this section, sensitivity of the sheet-shelf profiles to buttressing factor W (eq. (2.4)), temperature-related viscosity A (eq. (2.2)), and basal friction parameters c and m (eq. (2.3)) is assessed.

The next experiments were done at low resolution ($\Delta x = 2km$), not enough to capture adequately moving grounding line. Indeed, Pattyn et al. (2012) find a non-physical hysteresis of grounding line position as a function of ice viscosity. To bypass this hysteresis, all experiments were conducted from an unrealistically low viscosity parameter, typically $A = 1e^{-20}Pa^{-3}a^{-1}$. This value is chosen such as the sheet almost totally fills the domain and that decreasing A to the desired value makes the grounding line retrograde. Other parameters were fixed. Bedrock is $b = -x/500$, accumulation rate is 0.3m/yr, and no basal melting is applied.

3.1.1 Buttressing factor W

Figure 3.1 shows the influence of the buttressing factor W on both sheet and shelf. Not only the buttressing induces a migration of the grounding line, but also refrains the shelf from flowing freely. Ice can thus accumulate: at high buttressing factor (low shelf width), shelf becomes characteristically convex. This kind of profile is not encountered in nature and may be due, though this needs to be evaluated properly, to enhanced basal melting at depth.

As explained in introduction, buttressing is determining for grounding line migration induced by thinning of the shelf. At nil buttressing, melting below the shelf (of whatever amount)

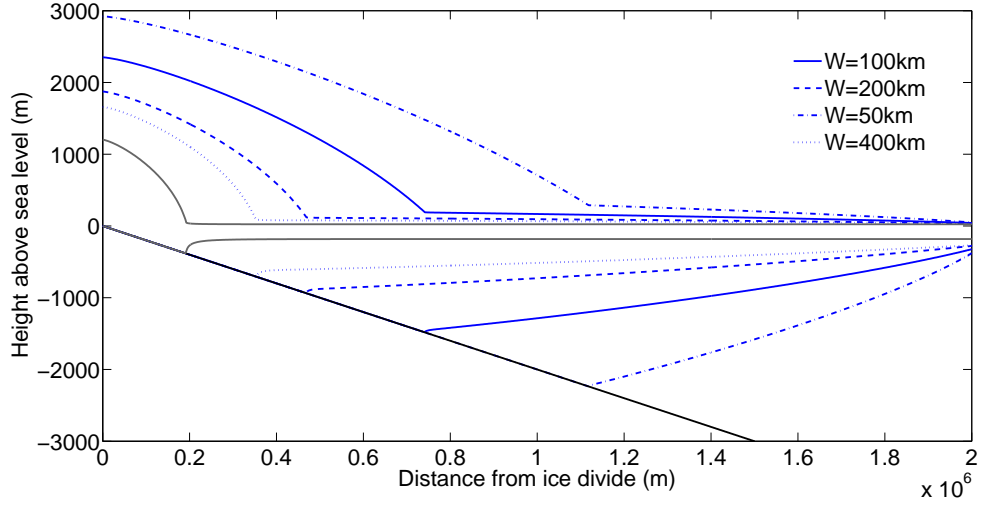


Figure 3.1: Influence of buttressing factor W (eq. (2.4)) on a marine ice sheet. $A = 1e^{-17}\text{Pa}^{-3}\text{a}^{-1}$, $c = 5e^6\text{Pa m}^{-1/3}\text{s}^{1/3}$, $m = 1/3$, $b = -x/500$. Grey profile is for nil buttressing.

only reduces shelf width, with no impact on the grounded ice at all. The end purpose of this thesis being to study the melt-induced grounding line migration, buttressing will be applied.

Noticeably, buttressing changes concavity in the vicinity of the grounding line. For relatively low buttressing, the slope is highest at the grounding line. Melting from the plume parametrisation will thus increase towards the shelf front (high buttressing) or show a peak near the grounding line (not shown). The former forces the plume parametrisation to maintain the convex shape; the latter tends to develop a positive melt-slope feedback. This will be discussed later, in section 4.1.

Foreseeing the coupling to the box parametrisation, this figure should be compared to Figure 3.8d, $w = 2W$). This figure shows that smaller buttressing, thus wider shelves, produces smaller melting. Therefore, grounding line retreat for large shelves would be limited both by reduce buttressing and smaller melt rate.

3.1.2 Viscosity parameter A

Influence of the viscosity parameter A is explored at Figure 3.3. This parameter depends on the crystal fabric, impurities and temperature (Weertman, 1983). Correspondence between A and ice

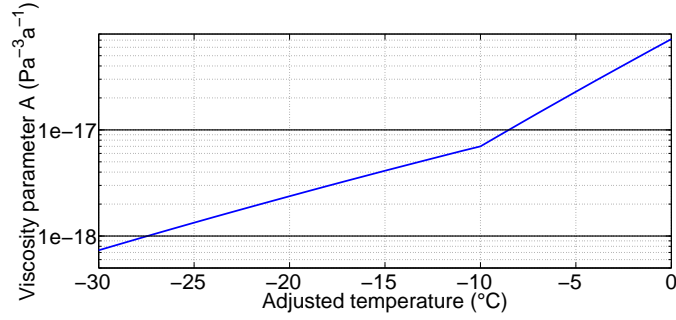


Figure 3.2: Dependence of ice viscosity on temperature

temperature is shown at Figure 3.2 according to (Pollard and DeConto, 2012a):

$$A = E \times A_{\pm} \exp\left(-\frac{Q_{\pm}}{RT_{\star}}\right)$$

where E is a fabric-dependant enhancement factor, fixed to 0.5; $A_{\pm} = 5.47 \times 10^{10}$ and $Q_{\pm} = 13.9 \times 10^4$ if $T_{\star} > 10^{\circ}\text{C}$, $A_{\pm} = 1.14 \times 10^{-5}$ and $Q_{\pm} = 6 \times 10^4$ otherwise; R is the gaz constant. T_{\star} is the depth-averaged ice temperature adjusted to pressure melting point.

The colder the ice, the higher the viscosity, and the higher must be the ice to allow for a same ice flux. Thus a low A implies a bigger sheet. At appropriate resolution (Pattyn et al., 2012), numerically resolved retreat of the grounding line is observed.

As for the buttressing parameter though to a lesser extent, the shape of the shelf is influenced by the viscosity parameter A . This parameter also contributes to determining the behaviour of the plume parametrisation (section 4.1).

3.1.3 Friction coefficients c and m

Sheet profiles for different c are shown in Figure 3.4. The friction parameter relates basal shear stress to velocity. The larger c , the smaller the velocity at a given shear stress. When ice is floating, the shear stress is nil, so the coefficient of the sliding law c and m do not influence the shelf per se. However, changes in basal law coefficient alter the sheet shape accordingly. An abrupt increase in c , for instance, first diminishes the grounded ice flux, hence a retreat of the grounding line. Then the sheet builds up and the grounding line closely recovers its initial state. Thus, c and m have almost no influence on the grounding line position.

To address more precisely the effect of the basal coefficients, Figure 3.5 shows a close-up of the grounding line for four different set of W , A , c and m . m takes the value of 1/2 and 1/3. c is

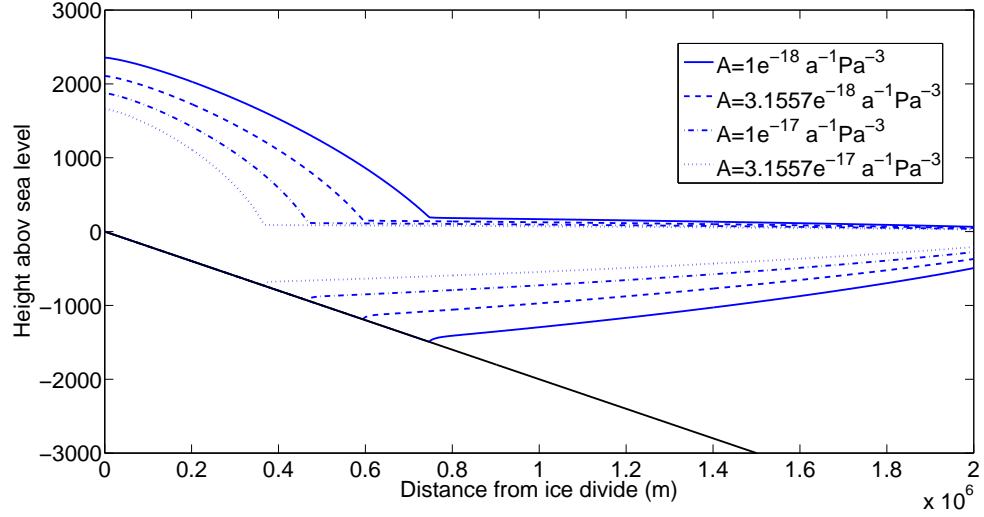


Figure 3.3: Influence of viscosity parameter A (eq. (2.2)) on a marine ice sheet. $W = 200\text{km}$, $c = 5 \times 10^6 \text{Pa m}^{-1/3} \text{s}^{1/3}$, $m = 1/3$, $b = -x/500$.

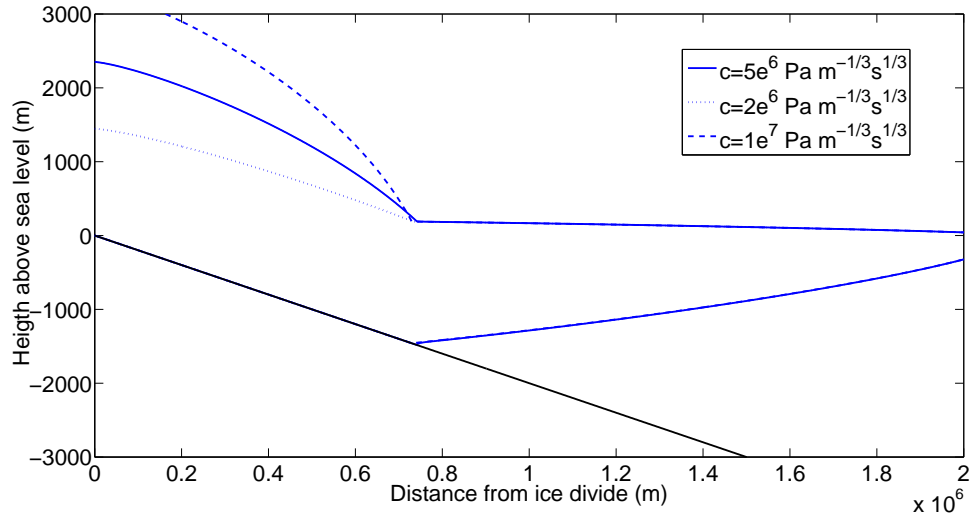


Figure 3.4: Influence of friction parameter c (eq. (2.3)) on a marine ice sheet. $W = 100\text{km}$, $A = 1 \times 10^{-17} \text{Pa}^{-3} \text{a}^{-1}$, $m = 1/3$, $b = -x/500$.

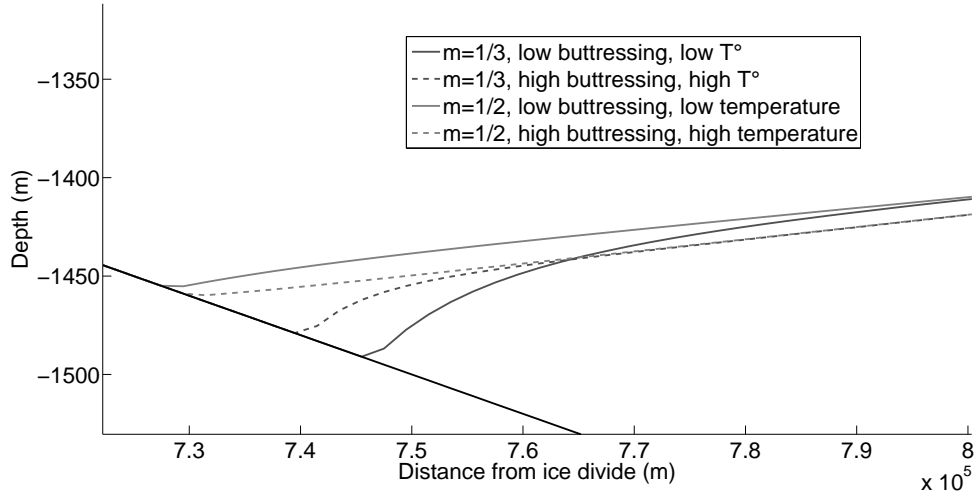


Figure 3.5: Close-up on the grounding line for 4 sets of W, A, m, c . The first point afloat is numerically incorrect because the "real" grounding line lies between it and the last grounded point and. Sliding law coefficients are $m = 1/2, c = 5 \times 10^7 \text{Pa m}^{-1/2} \text{s}^{1/2}$ or $m = 1/3, c = 6 \times 10^6 \text{Pa m}^{-1/3} \text{s}^{1/3}$. Buttressing and viscosity are $W = 100 \text{km}, A = 1 \times 10^{-17} \text{Pa}^{-3} \text{a}^{-1}$ or $W = 200 \text{km}, A = 1 \times 10^{-18} \text{Pa}^{-3} \text{a}^{-1}$. Bedrock is $b = -x/500$.

chosen accordingly to keep the height of the grounded ice approximately unchanged. For both values of m , two sets of A, W yielding close grounding line position are tested.

100km downstream the grounding line, the shelf depends only on A and W . This is a considerable distance for many real ice shelves ; thus m and c must be taken into account when studying shelf response to basal melting. This is in line with Pattyn et al. (2006) that highlights the sensitivity of grounding line migration to basal drag. Gladstone et al. (2012) further emphasize the impact of basal drag on grounding line migration, particularly at "coarse" resolution ($\gtrsim 1 \text{km}$).

Moreover, the resolution-dependant lowering of the first afloat gridpoint makes crucial a proper consideration of the basal slope. Indeed, $m = 1/2$ presents a downsloping shelf to which nor the plume model, neither its parametrisation can be applied properly. Slope shall thus either be smoothed at this location (calculated on a lower resolution), either care must be taken not to couple the plume parametrization blindly to any shelf.

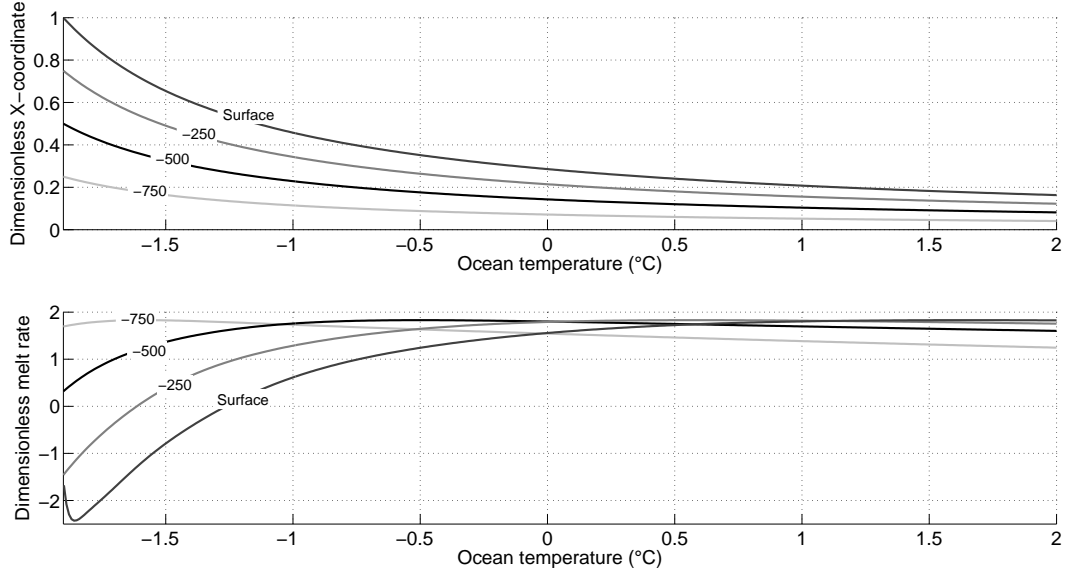


Figure 3.6: \hat{X} and \hat{M} against ocean temperature. $z_{gl} = -1000\text{m}$, $\alpha = 0\text{rad}$, $S_a = 34.65\text{psu}$. Contour lines represent different depths as measured from the sea level, so -750m is 250m above grounding line. Left border is surface freezing point (-1.922°C). Freezing point at the grounding line is -2.66°C .

3.2 Plume parametrisation

3.2.1 Dimensionless spatial coordinate

The dimensionless \hat{X} coordinate determines whether and where freezing can occur. It thus contains much of the physics of the plume. If it mostly depends on depth, local changes in slope or ocean temperature also have some influence on it. This is analysed in the following. Salinity will not be taken into account in the analysis. Indeed, its sole effect is through lowering of the freezing point, which is always compared to the ambient water temperature. As such, changes in salinity are equivalent to changes in temperature, with $\frac{dT_a^{eff}}{dS} = \lambda_1 = -5.73 \times 10^{-2}^\circ\text{C/psu}$. In the next sections, ambient temperature will often be referred to as a difference to surface freezing point, $T_a - T_f^{surf}$, so that the only remaining variable is depth. Unless stated otherwise, salinity will be 34.65psu .

As is shown in Figure 2.2, the geometrical factor that accounts for local slope in \hat{X} varies between 1 and 1.7728 and can thus not span the $[0, 1]$ range. More than half of the variability of

\hat{X} still has to be explained by T_a and z_b . The latter will be decomposed in two parts, namely z_{gl} , the grounding line depth, and Δz , the depth difference relative to the grounding line.

Figure 3.6 shows \hat{X} and \hat{M} as functions of ocean temperature for different Δz . Ocean salinity is 34.65psu, grounding line is 1km deep and local slope is nil. No refreezing can occur above -1.2°C. At high temperatures ($T_a > 0^\circ\text{C}$), melt path becomes much less sensitive to both depth and temperature. High temperatures are not likely to prevent \hat{X} to reach the peak value.

At lower temperature - and particularly when T_a approaches the pressure freezing point - sensitivity becomes larger. Vertical movement allows the plume to go throughout the entire melt curve. As has been said before (section 3.1.1), for a nil slope, the end of the universal melt curve is reached at the surface at the condition that $T_a = T_f^{surf}$, the left border of the graph.

As already discussed, the effect of slope is a dividing factor that readily diminishes the value of \hat{X} for given T_a and depths. As such, it will proportionally slow down the progression along the universal melt curve: lower temperatures or shallower depths will be needed to reach same dimensionless melt rates.

Depth of the grounding line has virtually no influence on the plume progression along the melt curve. More precisely, it does not affect the position along the melt curve reached by the plume at the surface. Indeed, at lowest possible temperature¹,

$$\frac{\partial \hat{X}}{\partial z_{gl}} = \frac{\partial}{\partial z_{gl}} \left\{ \frac{z_{surf} - z_{gl}}{\delta_T(\alpha) (z_{surf} - z_{gl})} \right\} = \frac{\partial}{\partial z_{gl}} \left\{ \frac{1}{\delta_T(\alpha)} \right\}$$

which is very close to zero (as shown by figure 2.2) because $\delta_T(\alpha)$ only depends on depth though pressure freezing point. At higher temperature, little sensitivity to z_{gl} is found, but is still very small as compared to plausible variations in slope or temperature. Tests have confirmed that grounding line depth has little impact on the distribution of melt, even at higher temperature (not shown).

For constant shelf edge depth and distance from grounding line, depth of the grounding affects absolute depth while keeping \hat{X} at the same relative position. It also increases difference to in situ freezing point, which is a prominent feature in the melt scale. This, as well as local slope, is investigated in the next section.

¹i.e. surface freezing point

3.2.2 Melt rate

Melt rate sensitivity to depth, temperature and slope is examined at figure 3.7 as the product of the dimensionless \hat{M} and the scale M . In this analysis, depth of the grounding line is arbitrary set at 1km below sea level. As a consequence to previous section, the depth axis can be read as relative vertical distance from the grounding line.

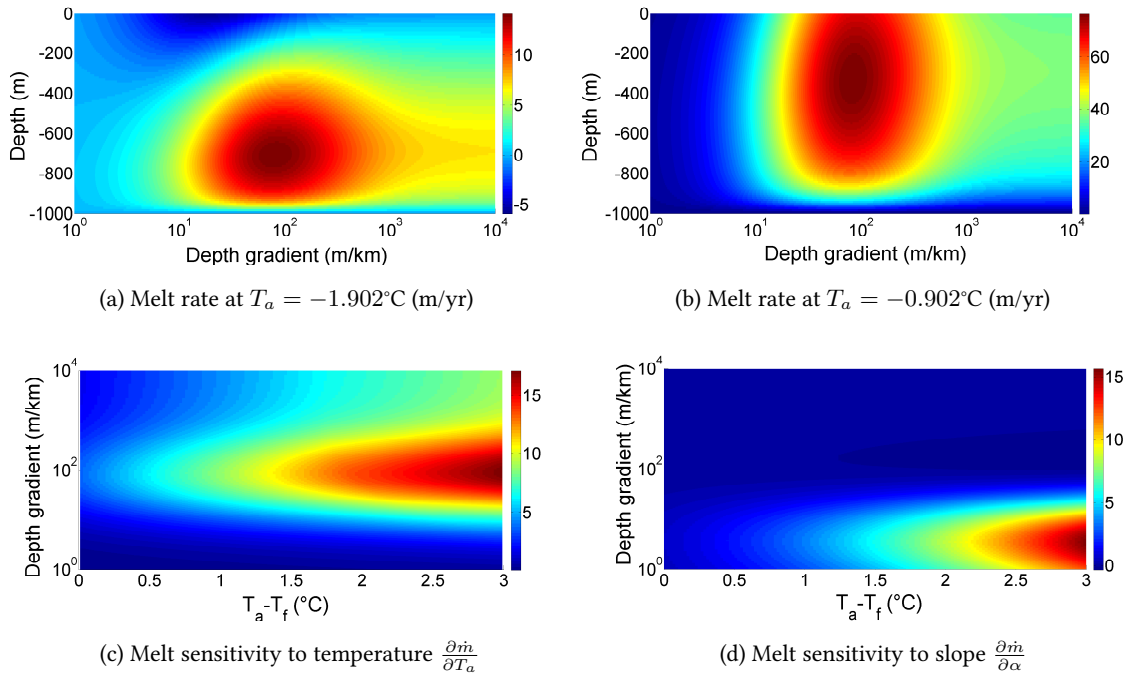


Figure 3.7: Melt rate sensitivity to depth, slope and temperature. (a) Melt rate along plume path at $T_a = T_f^{surf} = -1.902^\circ\text{C}$ (m/yr) (b) Melt rate along plume path at $T_a = T_f^{surf} + 1 = -0.902^\circ\text{C}$ (m/yr) (c) Sensitivity of maximum melt rate to a 0.1°C increase in temperature (m/(yr 0.1°C)) (d) Sensitivity of maximum melt rate to changes in local slope (m/yr/(m/km))

Figure 3.7a shows melt rate as a function of depth for a slope ranging from 0 to 84° (purely theoretical, can occur under instability). Profiles of real and modelled shelves are shown in Appendix A: they usually don't exceed 100m/km for a horizontal resolution of a few kilometers (cf. the dataset of A. Jenkins, provided together with the plume model). However, on-site surveys using autonomous underwater vehicles show a highly discontinuous, stair-like shelf base with local slope jumping from 0m/km to 1000m/km (50°) for 20 meters long between each terrace (Dutrieux et al., 2014) for the Pine Island Glacier.

At low temperatures, maximum melt rates occur for high slopes (near 100m/km) and in the first half of the vertical trajectory of the plume. As basal slope is usually larger in the vicinity of the grounding line than near the shelf front, this means that maximum melt is located near the grounding line, as expected. Refreezing is found near surface with relatively small slopes. At nil slope, refreezing begins 430m deep for $T_a = T_f^{surf}$ (Figure 3.7a).

At higher temperatures (Figure 3.7b), the plume does not develop the whole refreezing branch. No refreezing can occur and the effect of slope through $g(\alpha)$ in eq. (2.13) is dominant.

Increase in the maximum melt rate (wherever along the shelf it takes place) with respect to changes in ocean temperature is represented in Figure 3.7c. Sensitivity to temperature is found highest for large slopes ($\approx 100\text{m/km}$, case of Jakobshavn Isbrae or Pine Island Glacier). High temperature also increase sensitivity due to the power 2 to which temperature difference to surface freezing point is elevated.

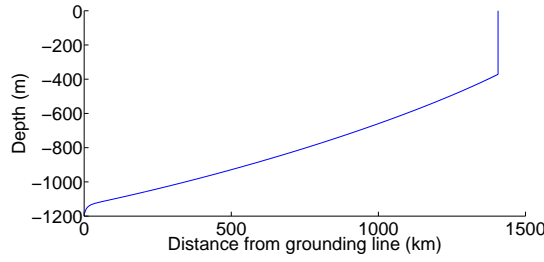
Basal slope depends on spatial resolution as lower resolution smooths out local features. Moreover, coupled sheet-shelf-ocean with the plume model parametrization involve a positive melt-slope feedback (section 4.1). As expected according to Figure 2.2, melt rate is most sensible to slope below 50m/km, with large sensitivity to temperature (Figure 3.7d).

3.3 Box parametrisation

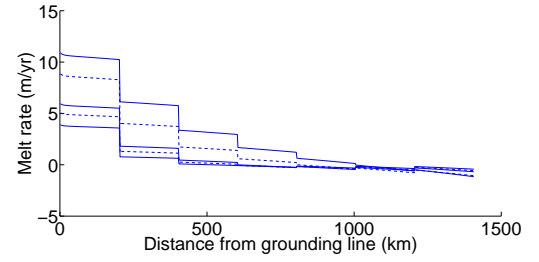
The overturning coefficient C , the effective turbulent exchange γ_T^* , and the width of the shelf w are parameters of the box parametrisation only. The first two can be tuned, while the latter will be imposed by the buttressing factor ($w = 2W$) in the coupled runs.

Figure 3.8 shows the distribution of melting below a non-coupled modelled shelf for different C , γ_T^* and w . The shelf is obtained for $A = 10^{-17}\text{Pa}^{-3}\text{a}^{-1}$, $W = 200\text{km}$, $c = 5 \times 10^6\text{Pa m}^{-1/3}\text{s}^{1/3}$ and $m = 1/3$ (section 2.1). It features a deep grounding line and a larger slope near the grounding line. This rapid variation of depth is surreptitiously reproduced in melt rate in the first box.

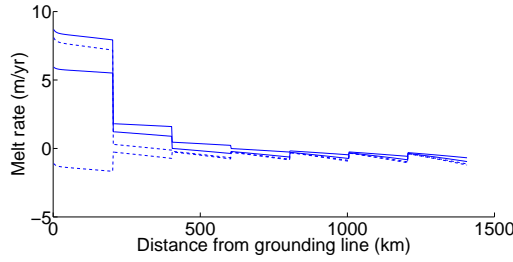
Figure (3.8b) shows sensitivity to C . The smaller the overturning strength, the smaller the melt rate. The whole melt pattern is smoothed, and eventual refreezing is also less important. This would suggest that larger water flows induce more melt at depth, freshen the plume more efficiently, which ultimately causes more refreezing.



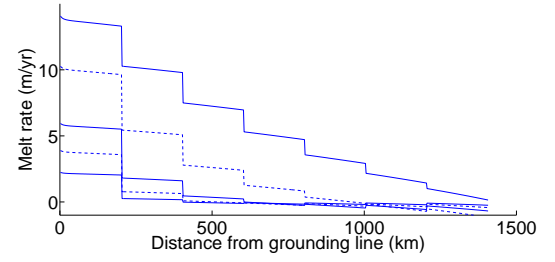
(a) Shelf base. The shelf is so long that $n_{box} > n_{max} = 5$, but this is not an issue.



(b) Sensitivity to overturning coefficient C . From bottom to top: $C = 5 \times 10^5$, $C = 7.5 \times 10^5$, $C = 10^6$, $C = 2.5 \times 10^6$, $C = 5 \times 10^6 \text{ m}^6 \text{ s}^{-1} \text{ kg}^{-1}$. $\gamma_T^* = 2 \times 10^{-5} \text{ ms}^{-1}$, $w = 200 \text{ km}$.



(c) Sensitivity to γ_T^* . From top to bottom in the first box: $\gamma_T^* = 2 \times 10^{-5}$, $\gamma_T^* = 6.32 \times 10^{-5}$, $\gamma_T^* = 2 \times 10^{-4}$, $\gamma_T^* = 6.32 \times 10^{-4} \text{ m/s}$. $C = 10^6 \text{ m}^6 \text{ s}^{-1} \text{ kg}^{-1}$, $w = 200 \text{ km}$.



(d) Sensitivity to basin width, keeping the buttressing factor constant (section 2.1). Width from top to bottom: $w = 10$, $w = 50$, $w = 200$, $w = 400$, $w = 800 \text{ km}$. $C = 10^6 \text{ m}^6 \text{ s}^{-1} \text{ kg}^{-1}$, $\gamma_T^* = 2 \times 10^{-5} \text{ ms}^{-1}$.

Figure 3.8: Sensitivity of the box parametrisation tested on a modelled non-coupled shelf base shown in (a) to: (b) Overturning coefficient C ; (c) Effective turbulent exchange coefficient γ_T^* ; and (d) Basin width. $T_a = T_f^{surf} + 1^\circ \text{C}$.

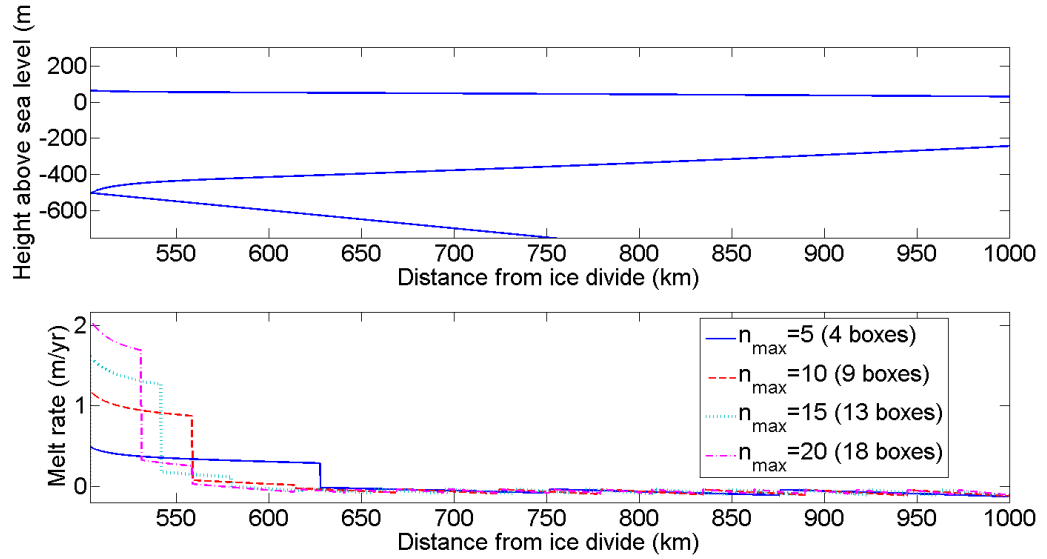


Figure 3.9: Distribution of melt according to the box parametrization as a function of the maximum number of boxes for rectangular shelves 400km wide. Domain length is 1000km, thus box length range between $\approx 16\text{km}$ ($n_{max} = 25$) to $\approx 100\text{km}$ ($n_{max} = 5$). $A = 10^{-17}\text{Pa}^{-3}\text{a}^{-1}$, $W = 200\text{km}$, $c = 2 \times 10^6\text{Pa m}^{-1/3}\text{s}^{1/3}$, $m = 1/3$.

There is little sensitivity to the effective turbulent exchange coefficient γ_T^* (Figure 3.8c) at low value. A shift occurs above $2 \times 10^{-4}\text{m/s}$, where the first box suddenly undergoes refreezing. This rapid shift towards unphysical refreezing provides a lower boundary for the choice of γ_T^* .

Basin width is an important factor in basal melt rate (Figure 3.8d). The narrower the basin, the higher the melt rate. This is expected to have consequences in the coupling to ice stream models. Indeed, the smaller the parameter W (accounting for the buttressing), the higher the buttressing and thus the longer the sheet (2.1, Figure 3.1). This would also affect melt rate towards larger value, showing thus a countervailing effect.

Walker et al. (2008) shows that both mean melt and spatial distribution of melt influence the grounding line retreat. Therefore, although Reese et al. (2008a) have chosen n_{max} (eq. 2.18) large enough so that mean melt rate converge, grounding line retreat is likely to depend on n_{max} . Distribution of melting along a non-coupled modelled shelf is shown at Figure 3.9. As melting is concentrated in the first box, the highest values of melt are found for the smallest boxes. This is further developed in section 4.2.

Chapter 4

Coupling sheet-shelf and oceanic models

This chapter deals with the precautions that must be taken when coupling the basal melt models into the coupled sheet-shelf model. The coupling experiment is presented in the next chapter.

Implemented melt models are linear and quadratic dependence on ocean temperature, the plume parametrisation and the box parametrisation. Unless stated otherwise, basal melting is always applied all of a sudden to sheet-shelf spin-ups obtained with no melting. This allows to study the reaction induced by changes in the shelf mass balance. This is critical in regard to the high instability encountered.

Also, the plume parametrisation is so unstable that it does not let the shelf expand if applied before reaching a slowly evolving state, while the box parametrisation does not always let a shelf develop. Finally, this is a simple way to apply the desired initial conditions, as they lead to different final state, at least for the plume model (Parizek and Walker, 2010).

The ice flow model being vertically-integrated, basal melting is included in the source term of eq. (2.5) below shelves. Salinity is kept at 34.65psu throughout the entire analysis, unless specified otherwise.

The basic idea is to produce steady-states of sheet and shelf with different values of W , A , c , m with a spatial resolution allowing for grounding line migration ($\Delta x = 200\text{m}$, Pattyn et al., 2012) and no basal melting. Unless specified otherwise, surface mass balance is $\dot{a} = 0.3\text{m/yr}$ across the entire domain. Applying basal melting of whatever model should make the grounding line

retreat. This should provide an estimate of grounding line retreat, grounded ice mass loss as a function of water temperature for different models.

In case of shelf front retreat, the boundary condition of eq. (2.6) is kept at the domain boundary. No calving front is thus parametrised when the shelf does not reach the domain boundary. Shelf thickness thus linearly decreases to the lower limit of 10^{-5} m, providing more buttressing than in case of buttressing.

When melting is so important that the shelf thickness reaches the minimum limit before the domain boundary, eventual remaining downstream patches of ice are suppressed. This can somehow be understood as the formation of an iceberg, though the process here does not contain ice fracturation, even parametrised, and does not describe calving per se. This reduces the length of the shelf and thus increases computational speed, at least for the plume parametrisation. Since the ice is so thin, buttressing factor is virtually nil, and the abrupt cutting of the shelf does not introduce discontinuity in the ice flux.

Melting is not applied to the first point afloat, whose height is incorrect and resolution-dependant because it effectively contains the "real" position of the grounding line.

4.1 Implementation of the plume parametrization

4.1.1 Numerical scheme

As was shown in section 3.2, the plume parametrization is very sensible to slope. This appears clearly in Figure 4.1 that shows melt rate along the shelf for $T_a = T_f^{surf}$. Wiggles near the shelf front (be it at the end of the domain, or when the shelf front advances within the domain boundaries) result from the conditions at the shelf front. Figure A.6.6 shows the slope of such a profile for three different numerical schemes tested. When applying melting from the plume parametrisation, melt rates are larger on the points where shelf base is lower, i.e. where ice thickness is larger. These wiggles thus tend to vanish under the plume parametrisation within ten years. This stabilisation requires a small time step, around $dt \approx 0.1$ yr for $dx \approx 2$ km, which also depends on ocean temperature. If time stepping or temperature are too important, the wiggles can either stay confined near the shelf front and show no evolution, either propagate as a wave towards the grounding line. Note that these time steps are comparable to those needed for 2D coupled runs throughout the entire Antarctica with f.ETISh (Pattyn 2017).

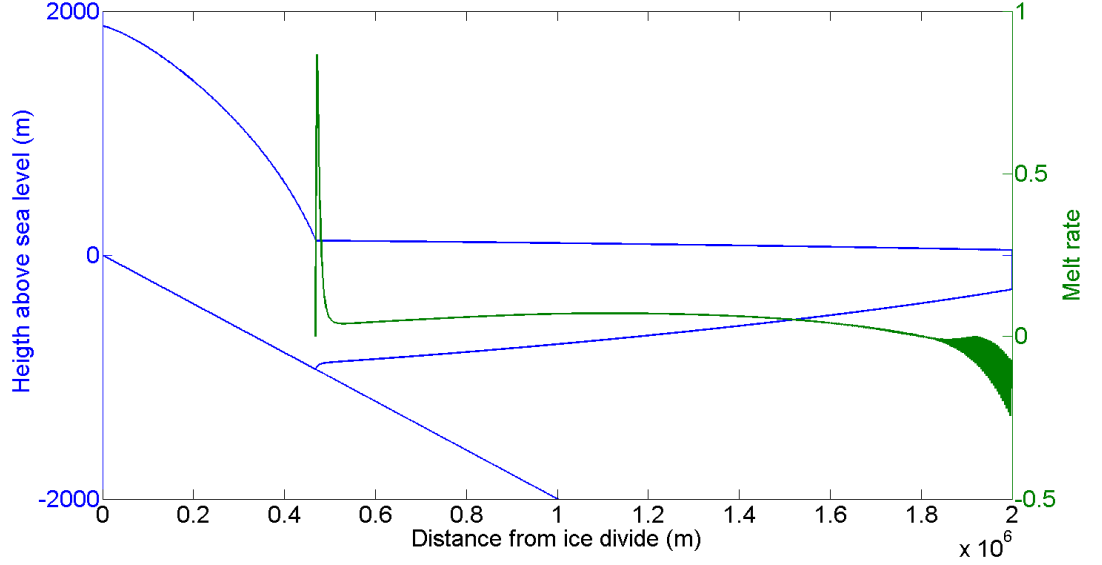


Figure 4.1: Melt rate along the plume path showing a melt peak confined at the grounding line and wiggles near the prescribed shelf front. $A = 10^{-17} \text{Pa}^{-3} \text{a}^{-1}$, $W = 200 \text{km}$, $c = 5 \times 10^6 \text{Pa m}^{-1/3} \text{s}^{1/3}$, $m = 1/3$, $b = -x/500$, $T_a = T_f^{surf}$.

Upwind scheme of first, second and third order were compared. Second order upwind scheme, that calculates slope as

$$\frac{\partial h_{b,i}}{\partial x} = \frac{-h_{i+2} + 4h_{i+1} - 3h_i}{2\Delta x}$$

and the 3rd order upwind scheme, in which slope is given by

$$\frac{\partial h_{b,i}}{\partial x} = \frac{-h_{i+2} + 6h_{i+1} - 2h_i - 3h_{i-1}}{6\Delta x}$$

stabilise the shelf front more slowly than the 1st order one:

$$\frac{\partial h_{b,i}}{\partial x} = \frac{h_{i+1} - h_i}{\Delta x} \quad (4.1)$$

The latter is thus preferred.

4.1.2 Ad-hoc corrections

Some features arising during coupled runs are not expected by the plume parametrisation. Near the grounding line, it can be that shelf base lies deeper than the grounding line (due to the set of parameters A , W , m and c , section 3.1.3, combined with high melt gradients). In such a case, $z_b < z_{gl}$ and $\hat{X} < 0$. The polynomial used to calculate the dimensionless melt scale \hat{M} is not valid

and would yield excessively small values. Negative values of \hat{X} are set to zero, which arbitrarily makes the melt rate null.

Instabilities near the shelf front, shelf base deeper than the grounding line, or carving of the shelf base forming small subshelf cavities share in common a negative shelf base slope. Negative slopes are supported neither by the plume model (because the plume lacks inertia) nor its parametrisation (because of square roots). At two dimensions, the plume would find a path towards decreasing depth. However, the second dimension is only implicit and expressed by the buttressing factor W . This assumes a rectangular shelf of constant thickness throughout the width. Assuming that the plume is forced to move away from the grounding line, the only direction it can follow in case of downsloping shelf is perpendicular to the ice flow. Accordingly, the effective slope would be taken as zero. This presents the disadvantage to ignore the physical process of melting.

Taking the absolute value of slope to get rid of the square roots empowers carving and instabilities by diminishing ice thickness in regions where ice is already "not thick enough", increasing the negative slope even more. Results after 10 years are plotted in Figure 4.2. To limit undesired perturbations by grounding line migration, the initial steady-state is coined using a depth-dependant melting law of the form

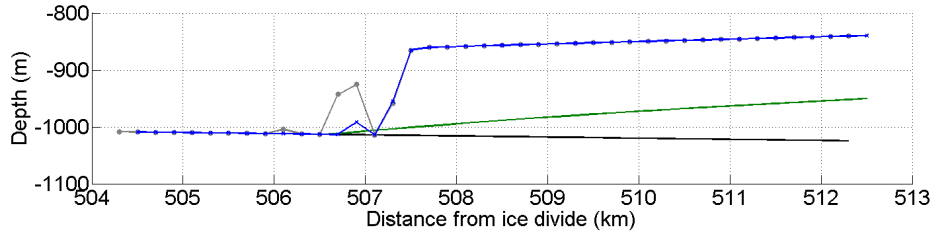
$$\dot{m} = \left(\frac{z_b}{1000} \right)^2 \quad (4.2)$$

which produces melt rates near 1m/yr near the grounding line. This also yields a shelf with a realistic concavity.

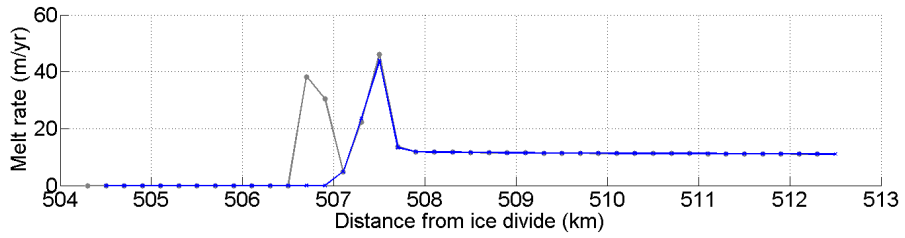
The formation of cavities upstream of the last grounded point is a consequence of the high concentration of melting near the grounding line. This is examined hereafter.

4.1.3 Melt-slope positive feedback

At relatively warm temperatures (depending on initial shelf profile), a dramatic increase in melt rate occurs confined within the vicinity of the grounding line because of a melt-slope positive feedback. The greater the local slope, the higher the melt rate at this point. Basal depth diminishes if the ice flow is too slow to compensate basal ablation of ice. Therefore, slope increases even more, accompanied by melt rate. At low resolution ($\Delta x \approx 2\text{km}$), stabilisation is observed (see Figure 4.3a). However, this can lead to combinations of numerical instabilities and cutting



(a) Shelf base near the grounding line



(b) Melt rate (m/yr) near the grounding line.

Figure 4.2: Shelf profile and corresponding melt rate for $\alpha = |\alpha|$ (grey line, dotted) and $\alpha = \max(\alpha, 0)$ (blue line, dotted) after 10 years of melting according to the plume parametrisation. Initial profile is shown in green. When melting is applied in the downsloping part of the cavities (grey), ice thickness further diminishes by a few hundreds of meters in the cavities within the next ten years (not shown). The grounding line lies near 506km. $\Delta x = 200\text{m}$, $T_a = T_f^{surf} + 1^\circ\text{C}$.

of the ice shelf¹ at high resolution ($\Delta x \approx 200\text{m}$). Moreover, the shelves slopes can be very high on only one grid point and thus depend on resolution.

Figure 4.3b shows a close-up on the grounding line. The grounding line is attributed to the last point where the two-gridpoints averaged height above floatation

$$h_{af} = \frac{b_i + b_{i+1}}{2} + \frac{h_i + h_{i+1}}{2} \frac{\rho_i}{\rho_w}$$

is positive. However, slope is so large here that the average is biased; the "real" grounding line is very close to the gridpoint $x = 509\text{km}$. Using a simple non-averaged height above floatation brings other complications.

This positive feedback (and subsequent cavity carving) also occurs under the coupling with the full plume model of Jenkins (1991). This is not surprising since Figure A.6.4 and Results 5.1

¹When melt rates are very high near the grounding line, ice thickness can reach the lower limit 10^{-5}m within a few kilometres. The downstream shelf is then suppressed.

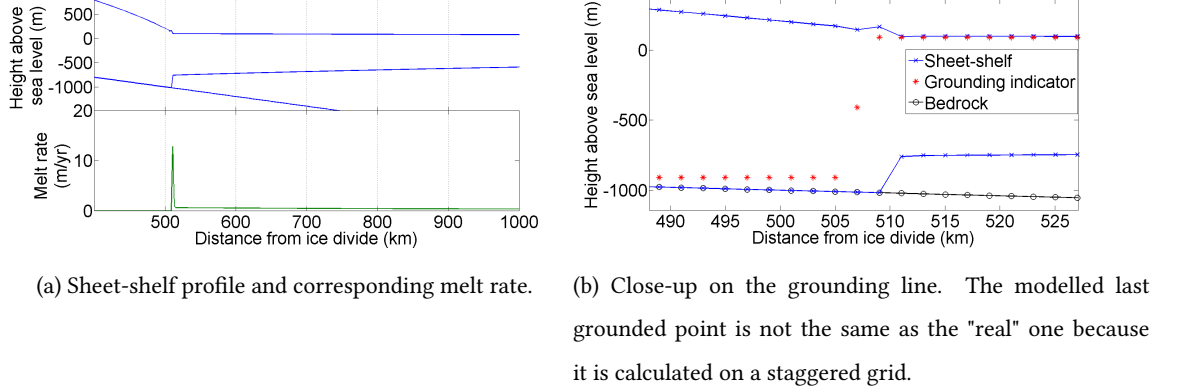


Figure 4.3: Steady-state profile and melt distribution at $\Delta x = 2\text{km}$ generated from the spin-up of eq. (4.2) at $T_a = T_f^{surf} + 1^\circ\text{C}$ when applying the uncorrected plume parametrisation. Slope at the first point near the grounding line reaches 128m/km , and falls to 4.3m/km on the next grid point.

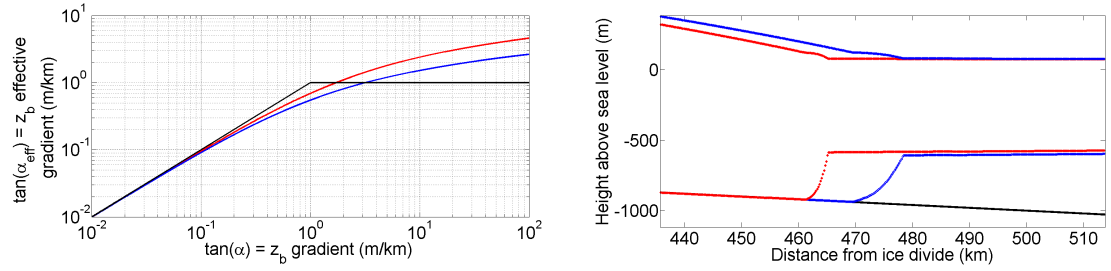
show that they agree well. However, as stated by Lazeroms et al. (2018), disagreement between the model and its parametrisation are larger when variations of slope are important, due to inertia which is not taken into account in the parametrisation. The feedback being a feature of the full model itself (coupled with the ice-stream model), any modification for the sake of stability will loose physical meaning.

In order to limit the melt-slope feedback, an effective slope α_{eff} is implemented in the calculation of $g(\alpha)$ for the melt scale M (not in the $\delta_T(\alpha)$ factor that locally adjusts the plume state). Two functions are tested (see Figure 4.4a) : a maximum value $\alpha_{eff} = \min(\alpha, \alpha^*)$ and a logarithmic saturation

$$\alpha_{eff} = \frac{\ln(1 + f\alpha)}{f} \quad (4.3)$$

The maximum value has to be lower than $\alpha^* = 10^{-3}\text{rad}$ to reduce significantly the instabilities. $f = 1000\text{rad}^{-1}$ is enough to globally prevent the formation of cavities upstream the last observed grounded point as in Figure 4.2. This points out a limit of this parametrisation to capture the dynamics of grounding line retreat when suddenly applying large increase in melting. However, no instability is observed for $f = 1000\text{rad}^{-1}$ at $T_a = T_f^{surf} + 2^\circ\text{C}$ and $dt = 0.01\text{yr}$, as opposed to lower values of f or higher temperatures².

²Remember that the supplementary 2°C are applied abruptly from a steady-state produced with much less melting



(a) Effective depth gradient as a function of depth gradient. (b) Grounding line at steady-state for the logarithmic saturation of slope. $T_a = T_f^{\text{surf}} + 2^\circ\text{C}$.

Figure 4.4: (a) Different implementations of the saturation of effective slope. (b) The logarithmic saturations (red: $f=1000$; blue: $f=2000$) stabilize the model, but not the maximum value $\alpha^*=10^{-3}\text{rad}$ (black line) at $T_a = T_f^{\text{surf}} + 2$. Maximum slope reaches 90m/km ($f=2000$) and 220m/km ($f=1000$), mean slope in the high sloping part is respectively 37m/km and 83m/km. Maximum melt rates are 12 and 27m/yr and immediately fall below 0.6m/yr in both case.

Figure 4.4a, and particularly α^* , are to be compared to observed and typical modelled slopes encountered (Figure A.6.3). The Pine Island Glacier, for instance, displays slopes much larger than 20m/km. Figure 3.6 shows that 2m/km lies in the lower part of the maximum sensitivity to slope, and does not reach the maximum sensitivity to temperature. For α^* must lie ways below these, this method is not considered acceptable.

The logarithmic saturation, by limiting the positive feedback, effectively smooths out the highest slopes. A close-up to the grounding line for a steady-state with $f = 1000$ is shown at Figure 4.4b. The smaller f , the steeper the slope next to the grounding line. This manner to limit slope still produces a very steep slope near the grounding line, that is only occasionally found in real shelves. Sensitivity to slope logarithmically saturated with $f=1000$ is shown at Figure A.6.7. Mainly, sensitivity is largest for smallest slopes.

Applied on the Pine Island Glacier, the saturation method using eq. (4.3) necessitates $f=350$ to feature a maximum melt rate of 85m/yr (Figure 4.5) and an average of 34m/yr. This is the melt rate obtained by mass conservation applied on the ice flow, based on satellite measurements and airborne observations, as mentioned by Dutrieux et al. (2013). These orders of magnitude are also obtained by ocean modelling (Payne et al., 2007; Jacobs et al., 2011; De Rydt et al. 2014),

near the grounding line (using eq. (4.2)).

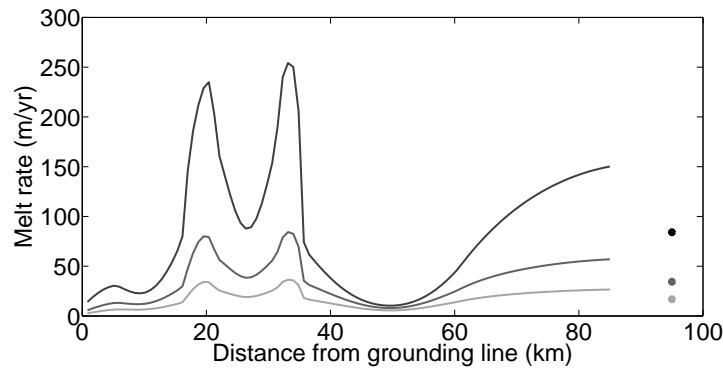


Figure 4.5: Melt rate below the Pine Island Glacier with saturation of slope as in eq.(4.3). Black: no saturation. Dark grey: $f=350$. Light grey: $f=1000$. Dots represent average melt rate.

while Rignot et al. (2013) reconstruct from radar interferometry a mean melt rate of $16\text{m/yr} \pm 1$. These studies work on different geometry (other transects or two horizontal dimensions), so a perfect agreement is not needed, particularly acknowledging the specific high spatial variability (Dutrieux et al., 2013) of melting in this basin³. However, this value of f is much smaller than the $f=1000$ required (see above) for the stability of the model⁴.

A more comprehensive comparison of the effect on saturation is given in Table A.6.2. As for the Pine Island Glacier plotted at Figure 4.5, the improvement is sensible. This method is thus considered appropriate.

Another way to smooth the slope and, thus, temper the melt-slope feedback was envisaged: averaging the slope in a number of boxes of given length. At high number of boxes, the melt-slope feedback is reproduced. At lower resolution, melting is often large enough to carve a hole in the first two box. Slope in the second box then becomes negative. Applying melt for negative slopes cuts the shelf. Using no melting, as previously chosen, lets the slope in the third box initiate another melt-slope feedback, which eventually cancels slope in the fourth box, and so on. This leads to serrated shelf base and melt distribution, which is judged unacceptable.

³The transect recorded in the dataset of A. Jenkins is not known.

⁴To globally mimic the PIG, experiment with $A=1.10^{-17}\text{Pa}^{-3}\text{a}^{-1}$, $\dot{a}=0.7\text{m/yr}$, $\Delta x=200\text{m}$, domain 200km long with downsloping bedrock $b=-x/500+100\text{m}$, $c=5.10^6$ and $m=1/3$, T_a and S_a as in Table A.6.1 was conducted. It turned out unstable even at $f=1000$, and showed a shape similar to Figure 6.6 at $f=2000$.

4.1.4 Flat shelf

Finally, as shown in Figure 4.4b, high melt rates near the grounding line produce a flat shelf until the domain boundary. The slope-dependant melt scale (eq. (2.13) and Figure 2.2) cancels for a nil slope, so the melt rate is uniformly 0 after the high-sloping region. Loss of buttressing is thus limited, long ice shelves can form even at high temperatures, and the melt distribution is not found in nature.

The approximation of no melting for nil slope comes from the absence of movement in the plume model (Jenkins, 1991). This is due to the use of the turbulent exchange coefficient $\gamma_T^* = \sqrt{C_d} \Gamma_T U$ which was found by Kader and Yaglom (1973) in the case of fully turbulent flows (see section 2.2.1). This is obviously not valid for low plume velocity.

As Holland et al. (2008) show, mean melt rate is proportional to the square of ocean temperature because it contains the product of the plume speed (depending linearly on the temperature difference to freezing point) and ocean temperature itself. This again involves the coefficient found by Kader and Yaglom (1973), but does not contain slope anymore. The quadratic melting law has been presented in section 2.2.4 and is used by Pollard and DeConto (2012).

It is thus assumed that when the plume parametrisation yields very low melt rates due to slope, a weak circulation might still develop. As its strength increases with temperature, the quadratic melting law makes sense. When it becomes even stronger, the overturning circulation described by the plume parametrisation is used. Thus the effective melt rate will be:

$$\dot{m}_{eff} = \max(\text{plume parametrisation}, \text{quadratic melting law}) \quad (4.4)$$

for each grid point.

4.2 Implementation of the box parametrization

In the coupled runs, the upgraded resolution within boxes is usually ignored, thus mean values are used over each box. Indeed, processing the high-resolution dramatically increases computational time for little improvement. An example of the changes both in shelf profile and melt rate distribution are shown in Figure 4.6.

Reese et al. (2018a) have built the box parametrisation using a maximum of 5 boxes per shelf. This number is large enough to reach convergence of the mean melt (see Figure A.6.8). However,

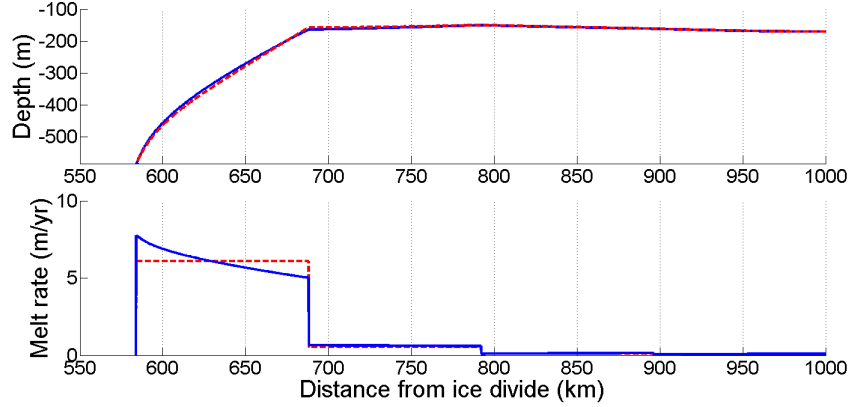


Figure 4.6: Steady-state changes between average and upgraded resolution in shelf shape obtained with the fully coupled model using the box parametrization and associated melt rates. Ocean temperature is $T_f^{surf} + 1^\circ\text{C}$. The grounding line has not moved.

this still largely changes the spatial distribution of melt (see Figure 3.9), which is also crucial. Reese et al. (2018b) show that a thinning of 1m applied locally on the shelf have far-reaching (up to 1000km far) impacts. The sensitivity of the global grounded ice to shelf thinning depends enormously on the location of this thinning.

Grounding line retreat and melt rate as a function of the number of boxes is shown at Figure 4.7. Melting is applied on a spin-up obtained at low resolution $\Delta x = 200\text{km}$ to capture grounding line migration on a linear bed of slope -1m/km . The maximum number of boxes (reached only by the longest shelves) suggested by the analysis of Reese et al. (2018a) is varied from 5 to 25 for four different ocean temperatures. In order to isolate the effect of melting distribution to the effect of change in the mass budget, the mass loss through melting is compensated by increasing the accumulation above the grounded ice. This also avoids "overshallowing" of the shelf.

Contrarily to what Reese et al. (2018a) have found, the mean melt rate does here show sensitivity to the number of boxes. Tests show that this is not due to the shape of the shelves (prescribed rectangular here, whereas the model is coined for semi-circular ones), neither to the choice of parameters C and γ_T (not shown). In this experiment, larger melt rates induce an advance of the grounding line because of the increased mass budget of the grounded ice. Melt rates then grow according to the deepening of the shelf. Figure A.6.9 show the final steady-state for $n_{max} = 5, 15$, and 25 at 1°C .

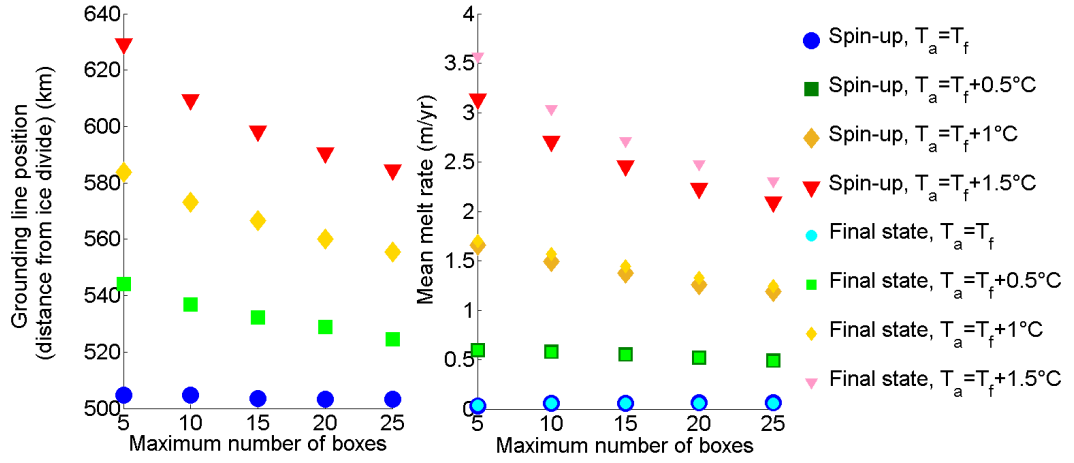


Figure 4.7: Sensitivity of grounding line retreat and initial and final mean melt rates as functions of number of boxes and for different temperatures. At 2°C, the shelf front doesn't reach the domain boundary and thus the boundary condition is not the same. Spin-up is shown at Figure 3.9.

Practically, the melt rate of the first box can be of an order of magnitude larger than melt rate in the second box. For relatively warm temperatures (as always, depending on the set of parameters), this can carve a hole on the shelf (this will be shown in section 5.2). Such a carving is the result of a combination of magnitude and extension of melting.

In case of retreating shelf front or cutting of the shelf, the region to which the melting is applied must be limited to an effective shelf, because the number and length of the boxes depend on the size of the shelf. Surface mass balance $\dot{m}_b = \dot{a} - \dot{m}$ (eq. 2.5) is cancelled above regions thinner than 1cm^5 . This value is larger than the minimum thickness to allow the unbuttressed flux of ice coming from the shelf to be evacuated at the domain boundary without involving melting. 1cm is probably not thought thick enough to present an hermetic barrier between the atmosphere and the plume; thus below this value, the ocean water is not controlled primarily by the plume. More importantly, this lies ways below the precision of the models.

⁵Keeping only the accumulation rate would eventually form a plane shelf that impacts the number of boxes.

Chapter 5

Results and discussion

5.1 Comparison between the models

The box parametrisation for different values of the overturning coefficient C and the effective heat exchange coefficient γ_T^* is compared to the non-saturated (section 4.1) plume parametrisation across the shelves provided together with the plume model of A. Jenkins (Table A.6.1; Figure A.6.1). Shelf width is set to 100km for every shelf. Only a subset of the entire ensemble is considered (Figure A.6.1), because many profiles are obtained by different interpolation methods, or do not start from the same point of a same transect (shown in Figure A.6.2). This way, double-counting is avoided.

Pine Island Glacier and Jakobshavn Isbrae are also excluded from the dataset for two reasons. The plume parametrisation yields extremely high melt rates (respectively, average of 84m/yr and 151m/yr) that are not even close to the estimations of Rignot et al. (2014) and Bernalles et al. (2016). Such high melt rates are only obtained locally (Dutrieux et al., 2013), which for a comparable resolution finds a maximum melt rate three times smaller. Moreover, melting beneath PIG and Jakobshavn Isbrae is an order of magnitude higher than the other shelves, so they mask their variations and "monopolise" the tuning. This lets us with 10 shelves.

Four statistics comparing the plume S_p and the box S_b parametrisations are calculated from the melt distribution and root mean square difference is evaluated according to:

$$\sigma = \sqrt{\frac{(S_p - S_b)^2}{10}}$$

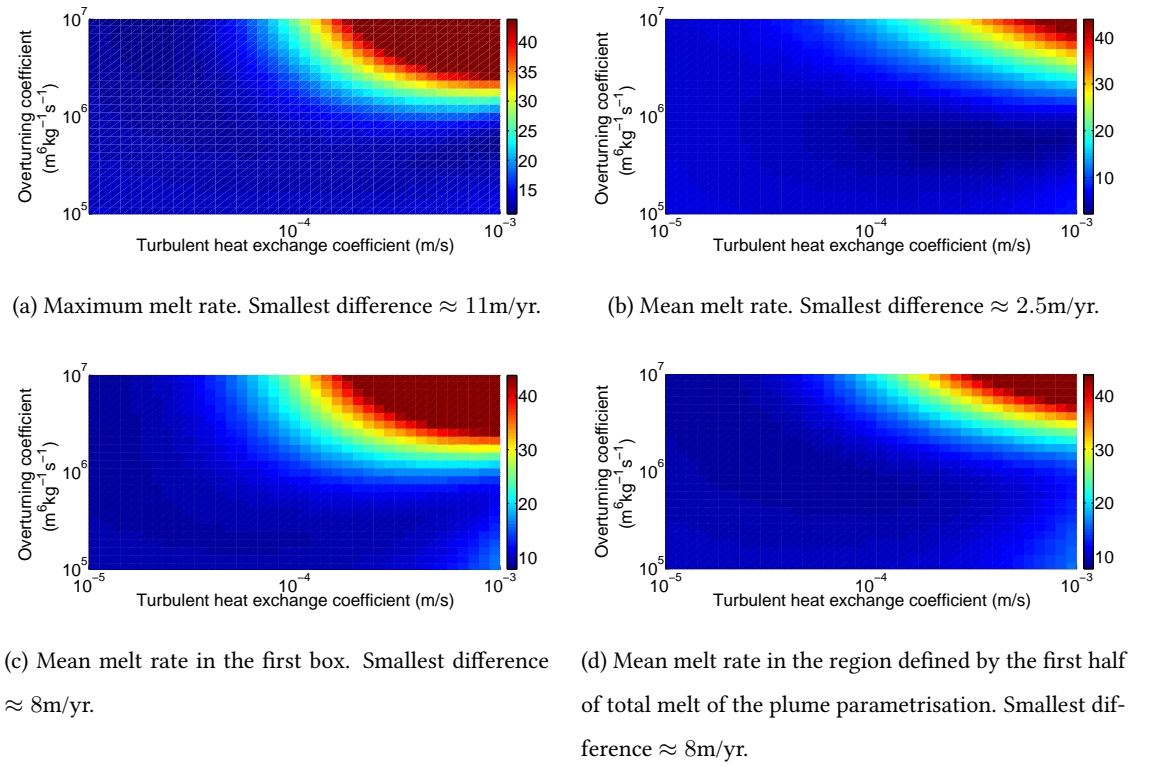


Figure 5.1: RMSD of four different statistics between the plume and the box parametrizations over the 10 selected shelves (see text) (zoom on the best match). Melt rates are limited to 45m/yr.

σ is plotted in Figure 5.1. Panel (a) shows the difference in the maximum melt rate, regardless its position along the shelf. Panel (b) shows the difference in melt rate at each grid point (each shelf being divided in 101 gridpoints to allow for standard comparison with the plume model of A. Jenkins). In panel (c), melting is averaged for both parametrisations in the region defined by the first box the box parametrisation. This is aimed to focus on the region of maximum melt rate, assuming that the peaks of melt may have different shapes, and yet be comparable if they peak in the same region.

In the same order of idea, one would define a peak of melt for the plume parametrisation. Although this is very clear in some cases, when slopes are high near the grounding line for instance, it is not always the case (see Figure A.6.4) because the distribution of melt is predominantly controlled by local slope rather than the position along the dimensionless \hat{X} -coordinate. Moreover, melting has more impact when it is concentrated near the grounding line. For these reasons, the "peak" of melt for the plume parametrisation is defined as the region between the grounding line and the point before which half of the total melting has occurred. Difference of mean melt rate in this region is represented in panel (d).

Only the mean melt rate shows a minimum (even beyond the range of values represented in Figure 5.1). Differences in maximum melt rate, mean melt rate in the first box and over the first half of the plume parametrisation melting decrease and stabilise at high C and small γ_T^* . This highlights that the two parametrisations give really different results, though on average they seem to concur. Nonetheless, melt peaks do never match, whatever the choice parameters.

Notwithstanding the rather good agreement (less than 5m/yr) for $3 \times 10^5 < C < 10^6$ and $2 \times 10^{-4} < \gamma_T^* < 10^{-3}$, remember that this was obtained from a subset of cavities with low slopes. The very large differences in the statistics between the two parametrisations for the Pine Island Glacier (where slopes of more than 50m/km are found) do not decrease significantly in this interval.

These RMSD should also be compared to the absolute melt rates. For the best matching parameters $C = 6 \times 10^5 \text{m}^6 \text{kg}^{-1} \text{s}^{-1}$ and $\gamma_T^* = 10^4 \text{m/s}$, the mean melt rate over the set of 10 glaciers given by the box parametrisation is 2.3m/yr, while the plume parametrisation yields 3.4m/yr. Discrepancies thus appear to be considerable.

These values of C and γ_T^* were chosen such as they minimize the root mean square difference in mean melt rates between the plume and the box parametrizations. γ_T^* should also not be

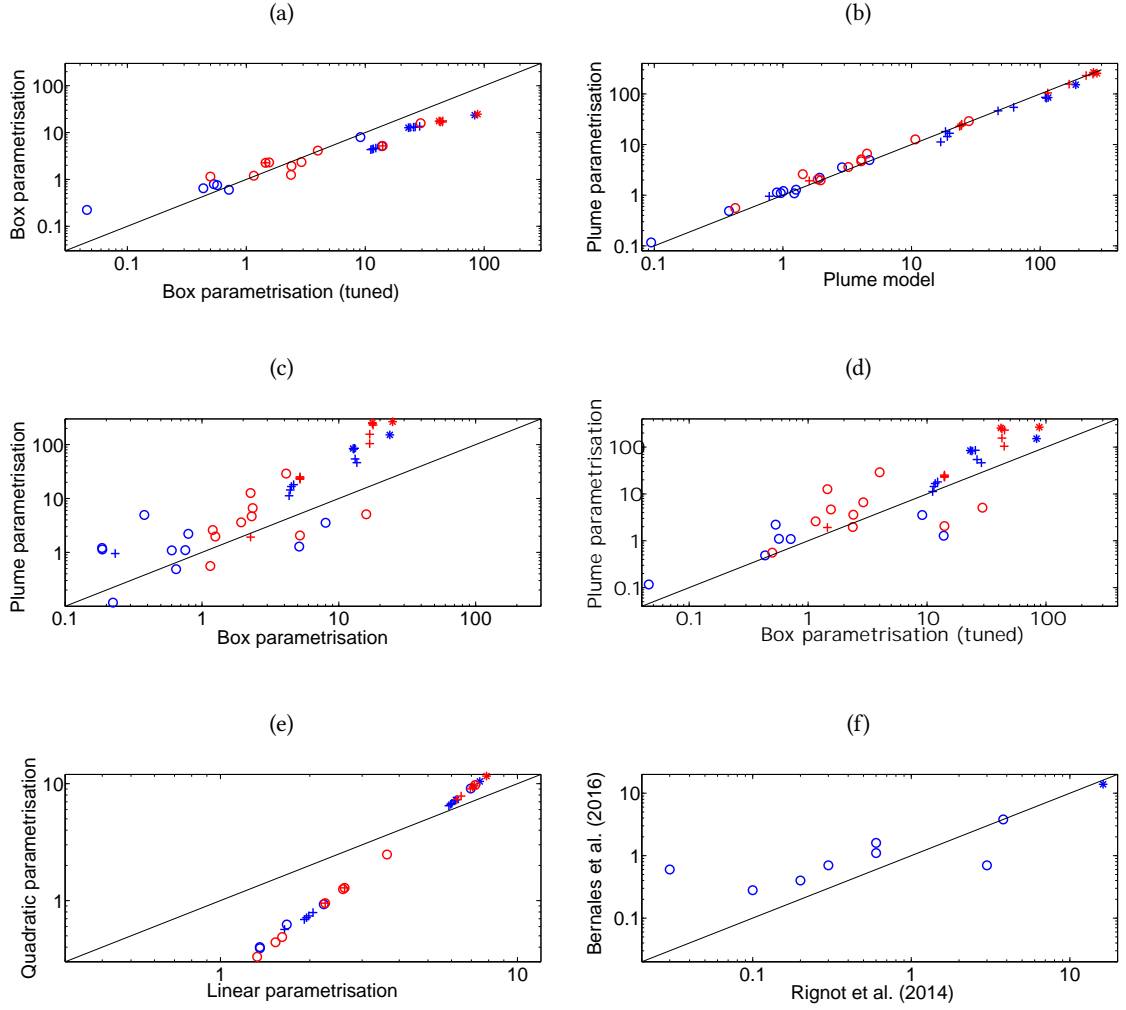


Figure 5.2: Comparison between the mean melt rate (blue) and maximum melt rate (red) for the 22 shelves of the dataset of Jenkins (m/yr). The plume model, the plume, box, linear and quadratic melting laws; for comparison, estimations of Rignot et al. (2014) and Bernales et al. (2016) are plotted against each other. Circles: Shelves used for the tuning (Figure 5.1). Stars: PIG and Jakobshavn Isbrae. Plus signs: the 10 excluded shelves (Figure A.6.2). Black line: 1 – 1 relation. Some negative data are not plotted.

too large in order to avoid that melt in the first box becomes negative or smaller than the in the second box (Figure 3.8c). This last condition is tested over the entire dataset of A. Jenkins. $C = 6 \times 10^5 \text{m}^6 \text{kg}^{-1} \text{s}^{-1}$ and $\gamma_T^* = 10^4 \text{m/s}$ are considered to give the best match with a mean difference 3m/yr. The melting they produce is shown in Figure A.6.4. As compared to the values chosen by Reese et al. (2018a), this mainly improves the adequacy for the Moeller Ice Stream, and

Jakobshavn Isbrae - which was not used for the tuning. Together with the Pine Island Glacier, these are the shelves with the steepest slope. Nevertheless, the latter does not show substantial improvement. Figure 5.2a compares the mean and maximum melt rates of the tuned and original box parametrisation. Anyhow, Figure 5.2b and 5.2c and 5.2d show that the plume parametrisation does not fit to the original neither the tuned box parametrisation, though the latter yields higher melt rates.

Nevertheless, it is not clear whether increasing mean melt rate from the box parametrisation is a benefit, as it would increase the deviation from the top-down approaches of Rignot et al. (2014) and Bernalles et al. (2016). These latter yield much smaller mean melt rates than does the tuned box model (Figure 5.2f; Figure A.6.2).

The sensitivity analysis performed by Reese et al. (2018a) for the box parametrization suggests values of C ranging between $5 \times 10^5 \text{m}^6 \text{kg}^{-1} \text{s}^{-1}$ and $7 \times 10^6 \text{m}^6 \text{kg}^{-1} \text{s}^{-1}$, and values of γ_T^* ranging between 1.5×10^{-5} and $3.5 \times 10^{-5} \text{m/s}$, so the dataset we use (that includes no warm cavity), the standardised shape of the shelves and the box delimitation influence the has a clear influence on melt rates.

While the plume parametrisation shows an excellent reproduction of the melt rates delivered by the plume model (Figure 5.2b), strong disagreement is obvious between the two parametrisations (Figure 5.2c and 5.2d). If the plume parametrisation often yields larger melt rates (particularly at high melt rates), this is not always the case. The differences being large despite the tuning, the original parameters C and γ_T^* are chosen¹. The two parametrisations shall thus not be readily compared one against another as they differ largely.

Figure 5.2a shows that the tuning of Figure 5.1 quite increases the largest melt rates of the box parametrisation. Average melting of up to 100m/yr are produced after tuning, whereas they were limited to less than 30m/yr in the original configuration. This shows that the proper choice of the parameters is of huge importance for describing the melting physics. However, little is known about the exact value of γ_{TS} (Jenkins et al., 2010), whereas Gwyther et al. (2015) point out the critical role it plays in the entire shelf cavity overturning circulation.

Figure 5.2e shows the linear (from Beckmann and Goosse, 2003) and quadratic (as in DeConto

¹Using a γ_T^* smaller than the maximum $1 \times 10^{-4} \text{m/s}$ also makes less likely freezing in the first box, as was observed during coupled experiments.

Constant	Value
A	$10^{-17}\text{Pa}^{-3}\text{a}^{-1}$
W	100km
c	5×10^6
m	1/3
\dot{a}	0.3m/yr
L	500km

Table 5.1: Value of the parameters used for the grounding line retreat experiment.

and Pollard, 2016) parametrisations that only depend on depth (section 2.2.4). Both are unable to yield maximum melt rate substantially larger than 10m/yr even for the Pine Island Glacier, highlighting the sensitivity of slope and depth of the plume and box parametrisations.

5.2 Grounding line retreat

Each four parametrisations described in section 2.2 are applied to a spin-up produced with no basal melting with $\Delta x = 200\text{m}$. Bedrock slope is $b = -x/500 + 100$. Ice grounded above sea level serves to prevent a total rapid disintegration of the sheet in order to study variations with temperature. Table 5.1 gives the parameters of ice used for the experiment. Initial shelf is shown at Figure 2.5a²

The initial ocean is unstratified, at surface freezing point $T_a = T_f^{surf}$ with $S_a = 34.65\text{psu}$. Then ocean temperature is increased by steps of 0.1°C . Each simulation is conducted for 10,000 years to let the system stabilize. Shelf profiles reached after each temperature step are shown at Figure 5.3. Grounding line retreat is summarized at Figure 5.4 as a function of ocean temperature. As the temperature changes are small, time steps of 0.1 year for the plume parametrisation, 1 year for the others showed sufficient to guarantee stability (section 4.1).

Melting from the box parametrisation (Figure 5.3) is so intense in the first box that it carves in the shelf a hole 100km long. Beyond 0.5°C above surface freezing point, the shelf is cut. The

²Figure 2.5b shows melt rates obtained from the four parametrisation for a ruthless increase of 1°C and 2°C at once. Here, such large and sudden increase in melt rate are not imposed.

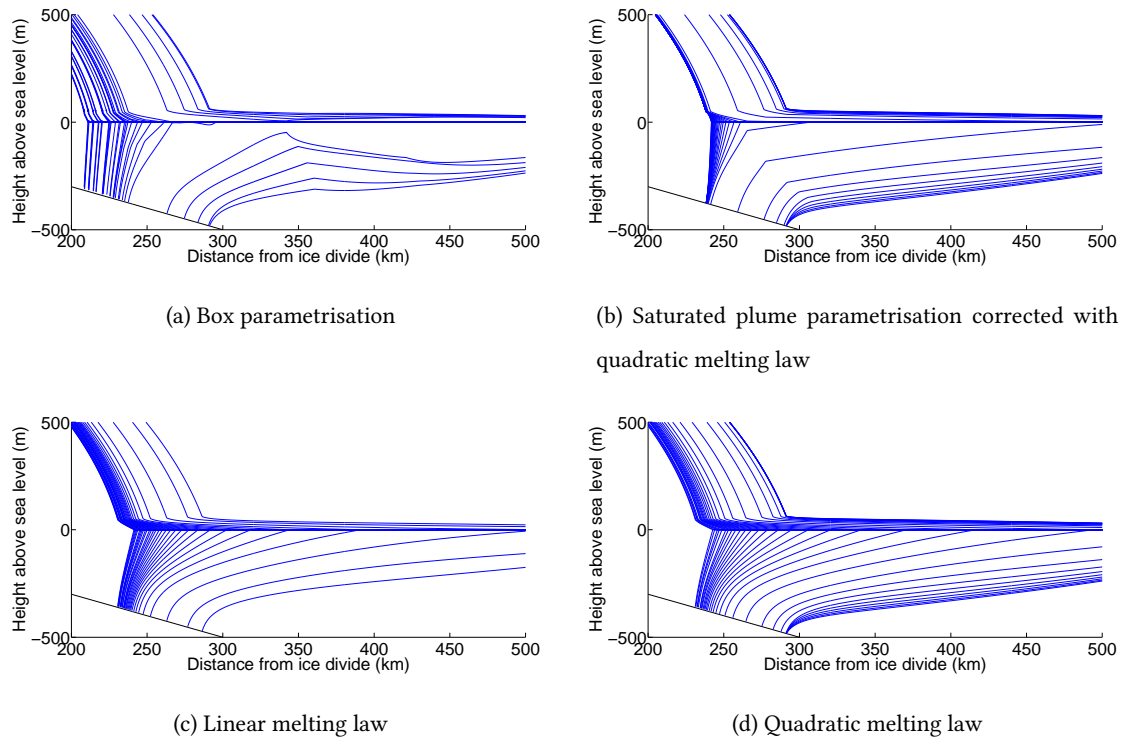


Figure 5.3: Shelf profiles for stepwise increase of ocean temperature.

buttressing is limited by the thin tongue connecting the forming "iceberg". The thinning of this tongue substantially reduces buttressing between 0.4°C and 0.5°C and grounding line retreats dramatically. The cutting is accompanied by a sudden switch from three boxes to two, which reduces the area over which depth is averaged, and thus increases melt rate in the first box.

The same is observed for the plume parametrisation augmented with the quadratic melting law at low slopes (Figure 5.3b). The saturated melt-slope feedback carves the shelf base within the first 10 to 15 kilometres after the grounding line. This diminishes slope downstream, where the quadratic melting law progressively consumes the shelf.

The same pathway is observed for the two polynomial melting laws (Figure 5.3c and d), with varying sensitivity.

The incapacity of the non-corrected plume parametrisation to melt flat shelves is responsible for the asymptotic grounding line retreat seen at Figure 5.4. At some point, warming the ocean increases melt rate in a very small region whose shortening cannot significantly reduce the residual buttressing of the 200m thick flat shelf. Shelf profiles obtained with the plume parametri-

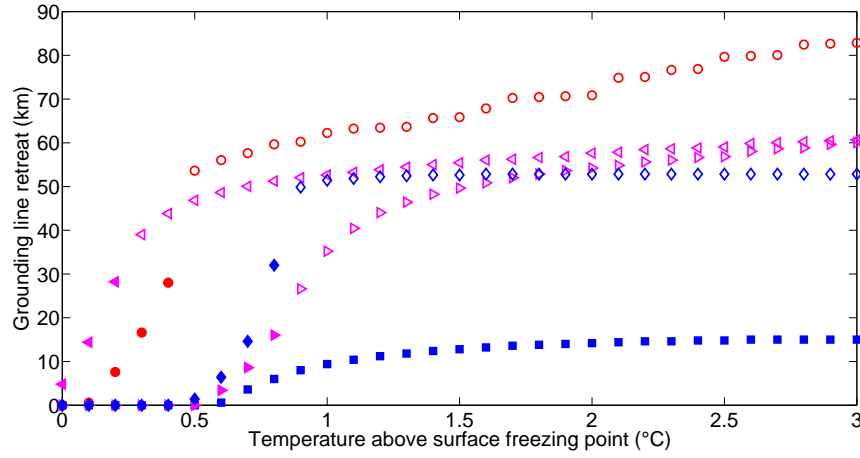


Figure 5.4: Grounding line retreat at steady-state after an increase in the forcing in subshelf melting. Red circles: box parametrisation; blue squares: saturated not corrected plume parametrisation; magenta left-pointing triangles: linear melting law; magenta right-pointing triangles: quadratic melting law; blue diamonds: saturated plume parametrisation corrected with quadratic for low slopes (eq. 4.4). Full shapes: shelf reaches the domain boundary (parametrised calving front). Empty shapes: shorter shelf (no calving front).

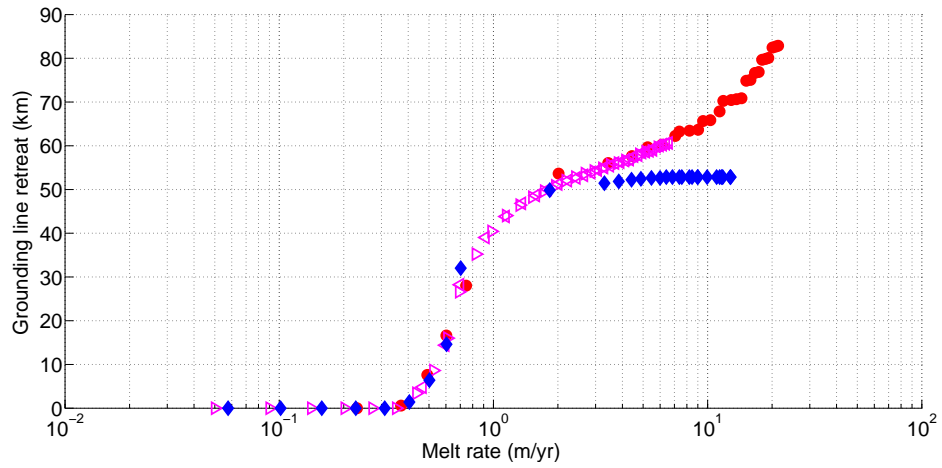


Figure 5.5: Grounding line retreat as a function of the mean melt over the first two thirds of the shelf (logarithmic scale). Initial grounding line position is 291.4km. Filled red circles: box parametrisation; empty magenta left-pointing triangles: linear melting law; empty magenta right-pointing triangles: quadratic melting law; filled blue diamonds: saturated plume parametrisation corrected with quadratic. The non-corrected plume parametrisation (not shown) follows the curve but is stacks at 0.6m/yr.

sation without the quadratic corrections for low slopes (section 4.1.4) are represented at Figure A.6.10.

Figure 5.5 shows grounding line retreat as a function of the mean melt rate calculated over the first two thirds of the shelf (from grounding line to domain boundary if reached, to first point of thickness smaller than 1cm otherwise). Grounding line does not retreat below an average melt rate of 0.4m/yr. The first jump takes place between 0.6m/yr and 0.7m/yr for all (except the non-corrected plume parametrisation, not capable to rise any further), retreating by 12km (box parametrisation) to 18km (plume parametrisation) at once.

Another 0.1°C increase makes these two reach 2m/yr on average with an additional retreat of respectively 18km and 25km. The plume parametrisation is helped by the melt-slope feedback, whereas the box parametrisation loses a box³

This retreat is mainly due to the balance between accumulation and ablation. Ice flux at the domain boundary is the total accumulation minus subshelf melting. For a grounding line at 260km, the shelf is 240km long. Mass balance at this point reads:

$$\int_0^{500} \dot{a} dx = \int_{260}^{500} \dot{m} dx$$

With $\dot{a} = 0.3\text{m/yr}$, mean melt is given by: $\bar{m} = \frac{500 \times 0.3}{240} = 0.62\text{m/yr}$. Above this value, the shelf front is forced to recede and buttressing decreases.

While the box parametrisation and the linear and quadratic melt laws continue to retreat due to weakened buttressing, the plume parametrisation ends up stuck. The reason probably lies in the distribution of melt. The three former undergo large or largest melt rates at depth. This rapidly thins the shelf, at constant (box parametrisation) or decreasing rate (the two others). This results in concave shelves (Figure 5.3b and c).

The plume parametrisation, however, must go through the dimensionless melt curve (Figure 2.1). The maximum of this curve is reached at $T_a = T_f^{surf} + 1.8^\circ\text{C}$. Increasing temperature makes the dimensionless \hat{X} coordinate recede towards 0.1 at $T_a = T_f^{surf} + 3.0^\circ\text{C}$. Ocean warming is counteracted by the plume which does not have time to mature. Melting is thus strongly limited next to the grounding line.

³The jump from two rather short boxes to a longer single box occurs instantaneously, leading to less stability of the shelf. The model hesitates between the two configurations at 0.6°C above surface freezing point. This is visible in Figure 5.3a)

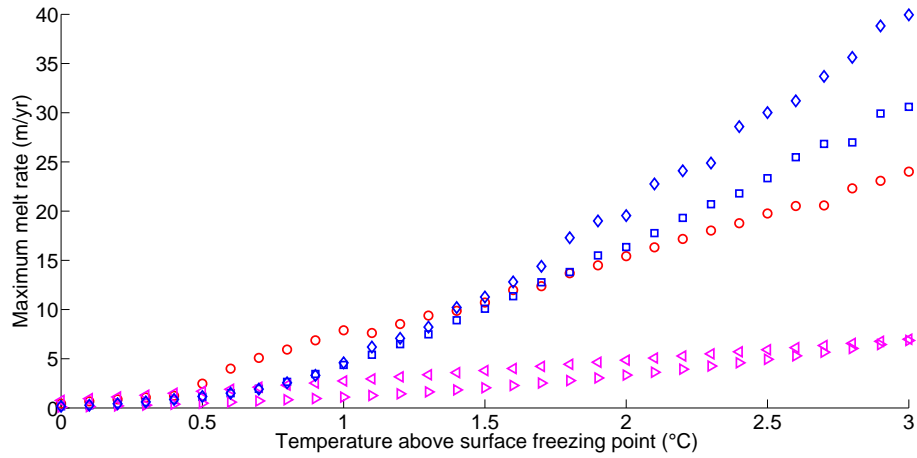


Figure 5.6: Maximum melt rate as a function of ocean temperature. Symbols as in Figure 5.4, but not filled.

As the plume develops, the maximum melt rate ultimately reaches 39m/yr, which is 10m/yr larger than the maximum melt rate of the box parametrisation and 30m/yr more than the linear and quadratic parametrisation (Figure 5.6). Nonetheless, shelf has already been able to significantly buttress the sheet, as shown by the convex shape of Figure 5.3b. At this point, the shelf of the plume parametrisation is only 4200m long.

Chapter 6

Conclusion

In this thesis, the plume parametrisation of Lazeroms et al. (2018) has been coupled for the first time to a flowline ice stream model with parametrised buttressing. The plume parametrisation is shown very unstable, requiring time steps typically $\approx 0.1\text{yr}$ for a spatial resolution of 200m. It is very sensible to local slope, and prone to develop unlimited melt-slope feedback, as the one dimensional plume model of Jenkins (1991) (Parizek and Walker, 2010) and a more sophisticated three dimensional thermohaline circulation (Walker and Holland, 2007). By saturating the effective slope, melt rates closer to other ocean models, parametrisation, and top-down estimates are found. The plume parametrisation is also incapable of dealing nil slopes, which is likely to be less handicapping in simulations with two horizontal dimensions.

Numerous tuning have been applied to the plume parametrisation in order to allow for the coupling, each of them scarifying a bit of the physics it contains. However, it was emphasized that the linear dependence of turbulent exchange coefficient on velocity might not deliver plausible results, at least in one explicit horizontal dimension.

The box parametrisation of Reese et al. (2008a) is shown to differ in any way from the plume one, as they could not be tuned to agree with each other. Means, maxima and spatial distribution of melting are different.

Applied as ablation term in an ice stream model, it is shown that dramatic retreat of the grounding line occurs whenever the mean melting rate over the shelf overcomes the total accumulation. This is thus specific to the imposed conditions. For a given ice stream model, the extent of retreat, however, depends on the melt distribution, as confirmed by Walker and Holland

(2007).

Consequently, maximum melt rate appears not determining at all. Retreat of the grounding line is shown much less sensitive to the forcing induced by the plume parametrisation than the three others. This seems to be caused by the relatively slowly increasing melt rate as the plume forms near the grounding line. Gladstone et al. (2017) find that such a melt distribution should show a better convergence with resolution; however the fixed grid used here imposes to keep a high spatial resolution (Vieli and Payne, 2005).

The results presented here can only raise attention to the existence of thresholds in melt-induced grounding line retreat for SSA models. SIA was not included, which introduces imprecision in capturing the grounding line motion (Pattyn et al., 2012). The whole set of ice creep, basal friction, buttressing and accumulation parameters have not been tested either. Importantly, the choice of a high constant basal friction coefficient c , abruptly set to 0 at the grounding line, exacerbate the need for a proper spatial resolution (Gladstone, 2012); but the analysis was performed at better resolution than recommended.

Regrettably, the present analysis does not address marine ice sheets grounded on downsloping bedrock inward. The participation of the melt sensitivity to depth in MISI could therefore not be evaluated. However, Gudmundsson et al. (2012) argues that MISI is stabilised under buttressing, before acknowledging (Gudmundsson, 2013) the counteracting effect of basal melting. Nevertheless, assessing the balance between the stabilising effect of buttressing and the destabilising effect of basal melting involves an explicit second dimension to accurately take buttressing into account.

Finally, some of the difficulties encountered - particularly linked to slope for the plume parametrisation - are likely to vanish in two horizontal dimensions. Jumping to 2D coupled models thus appears to be the next straightforward step in parametrising subshelf melting.

Appendix

The dataset of A. Jenkins is provided together with the plume model, and is comprised of the 22 glaciers gathered in Table 6.1, mainly in Antarctica (Figure 6.1). Exact transects are not known. 12 independent profiles were selected out of the 22 provided to avoid double-counting.

Shelf	Water temperature (°C)	Salinity (psu)	Difference to surface freezing point (°C)	Grounding line depth (m)
Amery Ice Shelf	-1.72	34.7	0.18	-2000
Brunt Ice Shelf	-1.66	34.5	0.23	-275
Ekstrom Ice Shelf	-1.66	34.70	0.25	-675
Erebus Ice Tongue	-1.83	34.95	0.09	-280
Central Ronne Ice Shelf	-1.76	34.82	0.15	-1405
Moeller Ice Stream (only two points) and five polynomial interpolations	-1.76	34.65	0.14	-1200
Western Ronne Ice Shelf and a 2-points linear interpolation	-1.76	34.82	0.15	-1425
Northern George VI Ice Shelf	1.17	34.67	3.07	-400
Jakobshavn Isbrae (Greenland)	1.10	33.87	2.96	-900
Pine Island Glacier and four short transects	0.46	34.55	2.36	-1300
Riiser-Larsen Ice Shelf	-1.66	34.53	0.24	-500
Ross Ice Shelf	-1.58	34.63	0.32	-520

Table 6.1: The 12 transects used in the model comparison and temperature, salinity and grounding line depth. Temperature and salinity are obtained from Reese et al. (2018a), Table 2 if available or Figure 2, plus the dataset of A. Jenkins for Jakobshavn Isbrae.

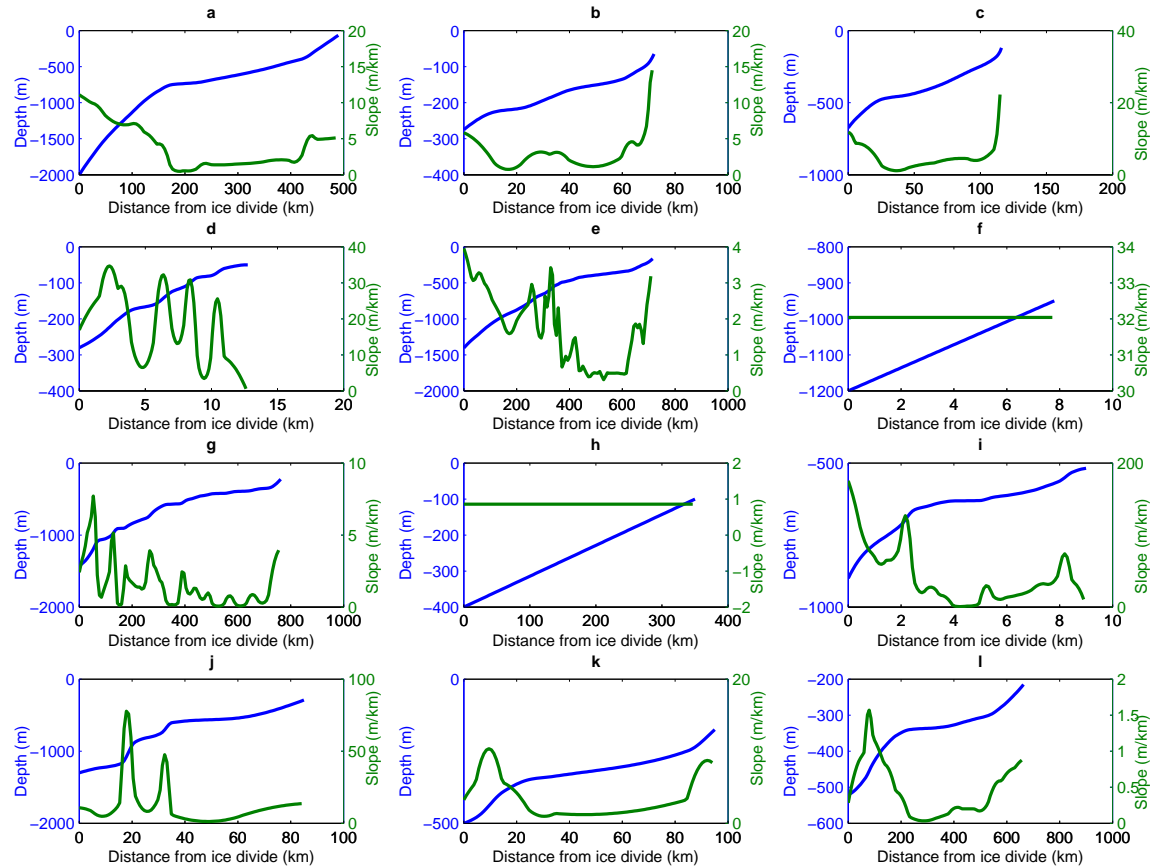


Figure 6.1: Depth of shelf base and slope for the 12 independant shelves available in the dataset of A. Jenkins. Data are interpolated to 101 points using piecewise cubing hermite interpolation. (a) Amery Ice Shelf (b) Brunt Ice Shelf (c) Ekström Ice Tongue (d) Erebus Glacier Tongue (e) Central Ronne Ice Shelf (f) Moeller Ice Stream (g) Western Ronne Ice Shelf (h) Northern George VI Ice Shelf (i) Jakobshavn Isbrae (j) Pine Island Glacier (k) Riiser-Larsen Ice Shelf (l) Ross Ice Shelf

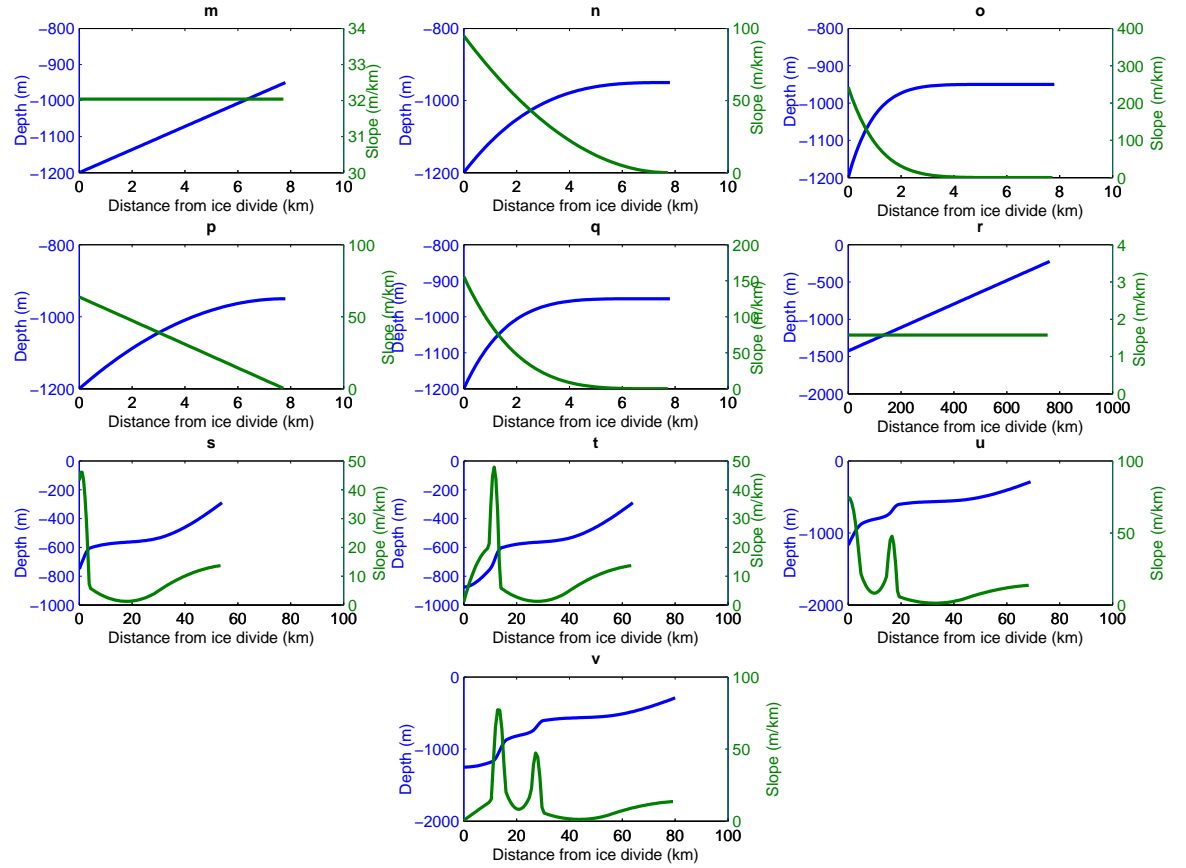


Figure 6.2: Depth of shelf base and slope for the 12 independant shelves available in the dataset of A. Jenkins (Part 2). Data are interpolated to 101 points using piecewise cubing hermite interpolation. (m) Moeller Ice Stream, 2nd-order interpolation (n) Moeller Ice Stream, 3rd-order interpolation (o) Moeller Ice Stream, 8th-order interpolation (p) Moeller Ice Stream, 4th-order interpolation (q) Moeller Ice Stream, 5th-order interpolation (r) Western Ronne Ice Shelf, linear interpolation (s-v) Pine Island Glacier, shorter transects

Shelf	pm	pp	ppsatsat	bp	bpt	BG	PC	Rignot	Bernales
Amery	4.7	4.9	1.0	0.4	-0.05	1.7	0.6	0.6 ± 0.4	1.6
Brunt	0.4	0.5	0.2	0.6	0.4	0.8	0.1	0.03 ± 0.2	0.6
Ekstrom	1.9	2.2	0.6	0.8	0.5	1.2	0.3	0.6 ± 0.2	1.1
Erebus	1.2	1.1	0.2	0.6	0.7	0.4	0.03		
Central Ronne	0.9	1.1	0.4	0.2	-0.05	1.4	0.4	0.3 ± 0.1	0.7
Moeller	18.4	18.1	2.8	4.6	12.3	2.1	0.8		
Western Ronne	1.0	1.2	0.4	0.2	-0.04	1.4	0.4	0.3 ± 0.1	0.7
Northern George VI	2.9	3.5	2.2	8.0	-9.1	7.0	9.1	3.8 ± 0.7	3.8
Jakobshavn Isbrae	189.1	151.6	23.4	23.6	83.3	7.5	10.5		
Pine Island Glacier	115.4	84.5	16.8	12.7	23.1	6.2	7.3	16.2 ± 1	13.9
Riiser- Larsen	1.0	1.1	0.3	0.8	0.6	1.0	0.2	0.2 ± 0.2	0.4
Ross	0.9	0.1	0.1	0.2	0.05	1.3	0.3	0.1 ± 0.1 (weighed mean)	0.28 (weighed mean)

Table 6.2: Mean melt rates (m/yr) from the different models considered, compared when available to reconstructed data from surface interferometry (Rignot et al., 2013) and calibration of a SIA-SSA model (Bernales et al., 2017). pm: plume model; pp: plume parametrisation; pmsat: saturated ($f=1000$); bp: box parametrisation; bpt: tuned; BG: Beckmann and Goosse (2003) (section 2.2.4; PC: Pollard and DeConto (2012) (ibid.).

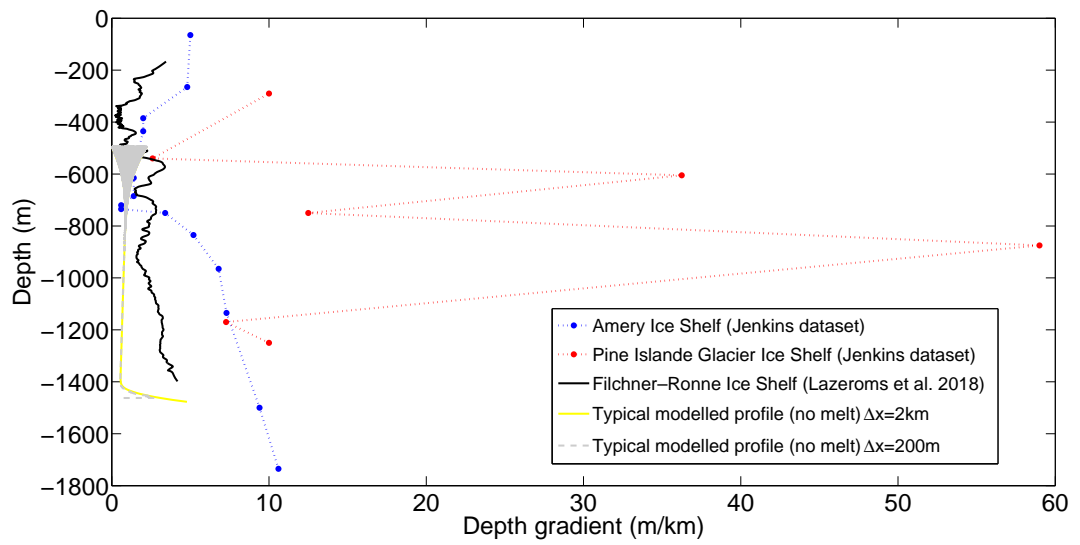


Figure 6.3: Profiles of different shelf in depth-slope space. Slope is calculated with the first-order scheme (eq. (4.1)). The grey funnel shape is due to numerical errors near the shelf front in absence of basal melting.

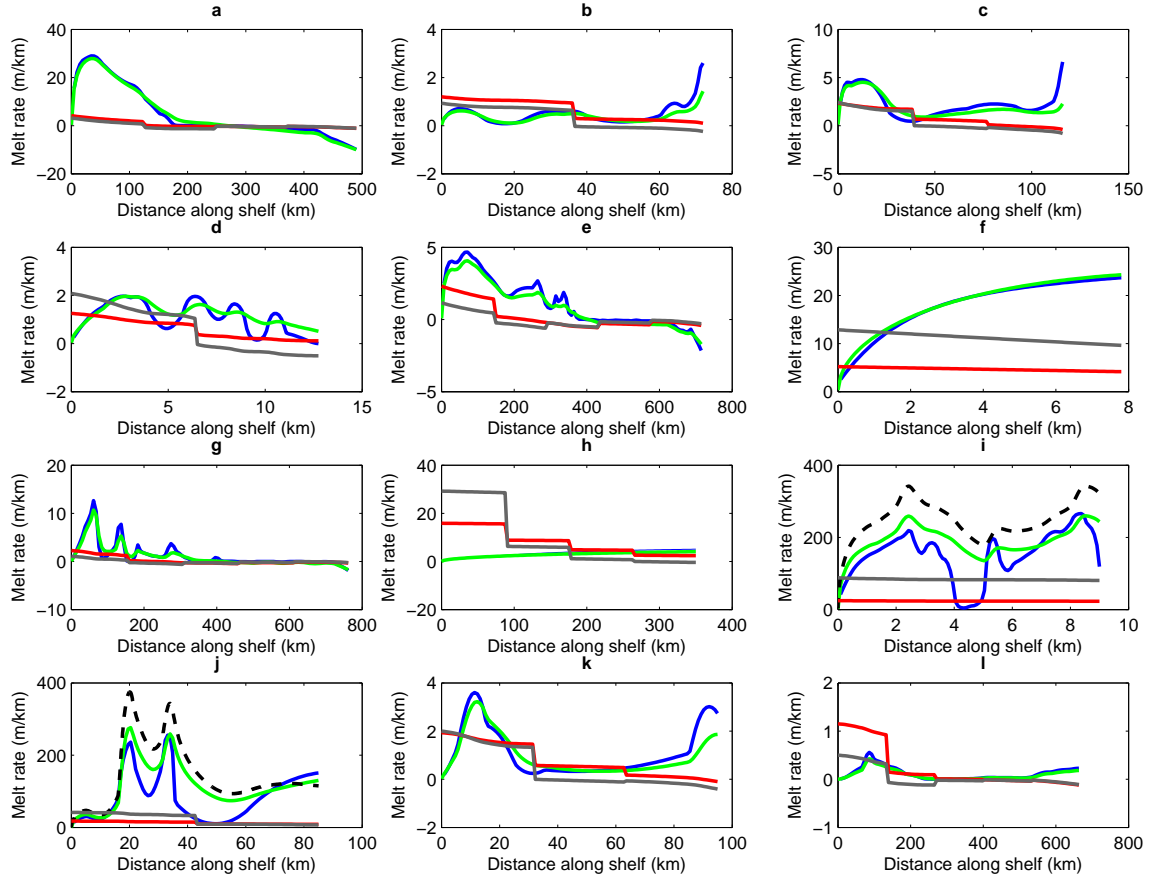


Figure 6.4: Melt distribution along the shelves shown in Figure 6.1 and the unstratified T-S data from Table 6.1. Red: box parametrisation, original C and γ_T^* (shelf width=100km); grey: box parametrisation, tuned parameters (section 5.1); light green: plume model; blue: plume parametrisation; black dashed (PIG and Jakobshavn): plume model with stratified ocean (T-S from A. Jenkins dataset). (a) Amery Ice Shelf (b) Brunt Ice Shelf (c) Ekström Ice Tongue (d) Erebus Glacier Tongue (e) Central Ronne Ice Shelf (f) Moeller Ice Stream (g) Western Ronne Ice Shelf (h) Northern George VI Ice Shelf (i) Jakobshavn Isbrae (j) Pine Island Glacier (k) Riiser-Larsen Ice Shelf (l) Ross Ice Shelf

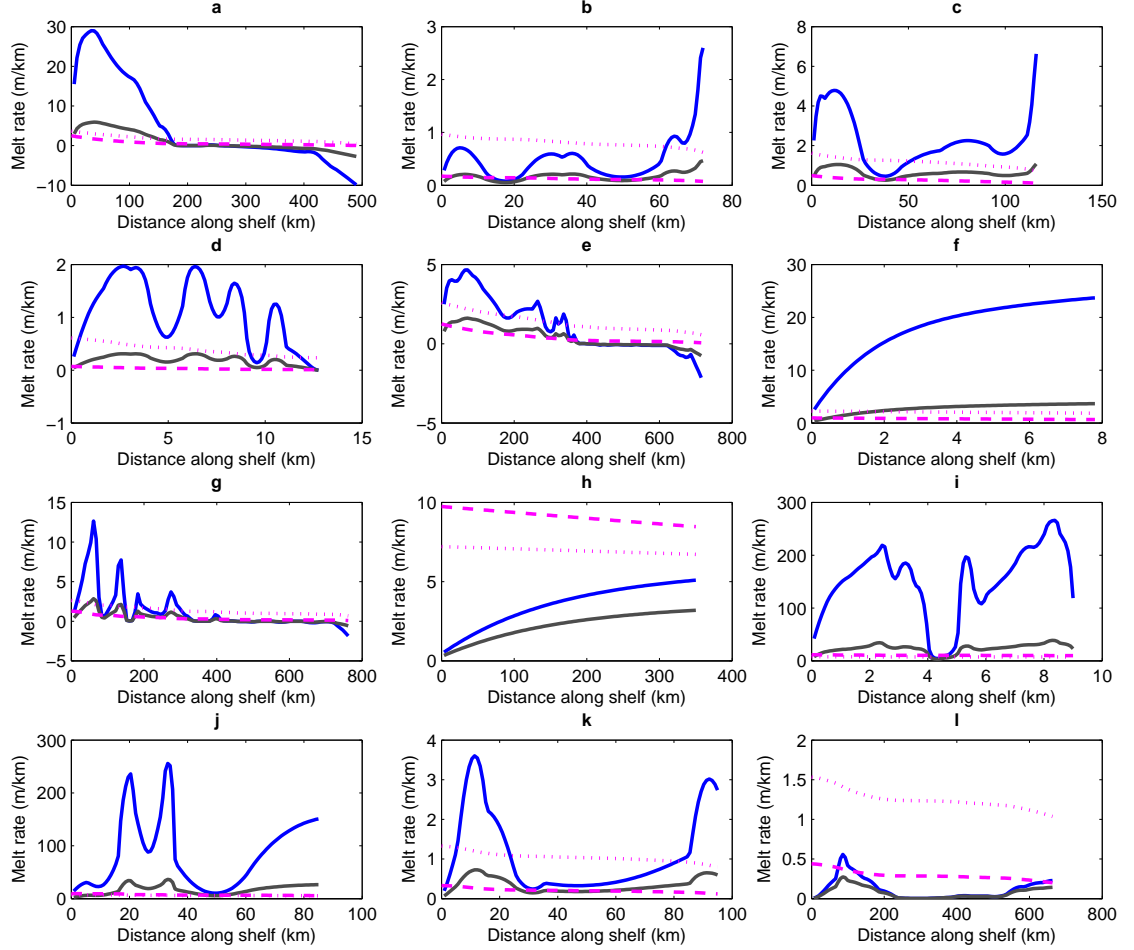


Figure 6.5: Melt distribution along the shelves shown in Figure 6.1 and the unstratified T-S data from Table 6.1. Magenta, dashed: quadratic melting law, as in Pollard and DeConto (2012); Magenta, dotted: linear melting law, as in Beckmann and Goosse (2003); blue: plume parametrisation; grey: plume parametrisation with logarithmic saturation $f=1000$. (a) Amery Ice Shelf (b) Brunt Ice Shelf (c) Ekström Ice Tongue (d) Erebus Glacier Tongue (e) Central Ronne Ice Shelf (f) Moeller Ice Stream (g) Western Ronne Ice Shelf (h) Northern George VI Ice Shelf (i) Jakobshavn Isbrae (j) Pine Island Glacier (k) Riiser-Larsen Ice Shelf (l) Ross Ice Shelf

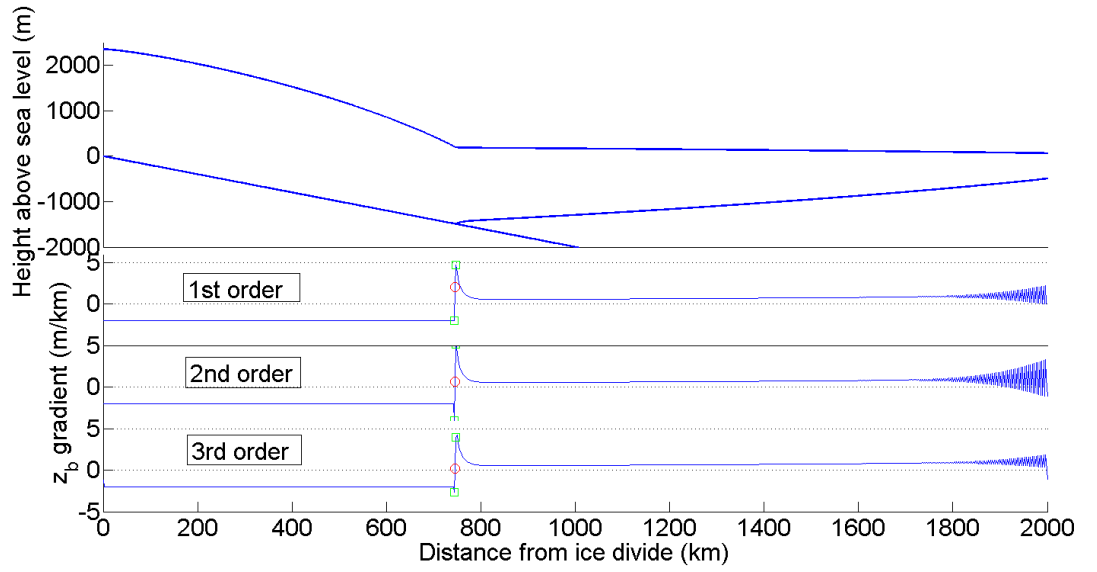


Figure 6.6: Steady-state sheet-shelf profile and slope values for the three numerical schemes tested (see text). Slope value at the last grounded point is red circled, previous and following are in a green square. The second order upwind difference maximises the wiggles in slope (thus melt rate) near the shelf front, that will stabilise more rapidly the shelf and at larger temporal resolution. However, the peak near the grounding line is even more acute and can eventually trigger instabilities, negative shelf basal slopes or cutting of the shelf. The steady-state is produced with no basal melting, $A = 1e - 18 \text{Pa}^{-3} \text{a}^{-1}$, $W = 200 \text{km}$, $c = 5e6 \text{Pa m}^{-1/3} \text{s}^{1/3}$, $m = 1/3$, $b = -x/500$.

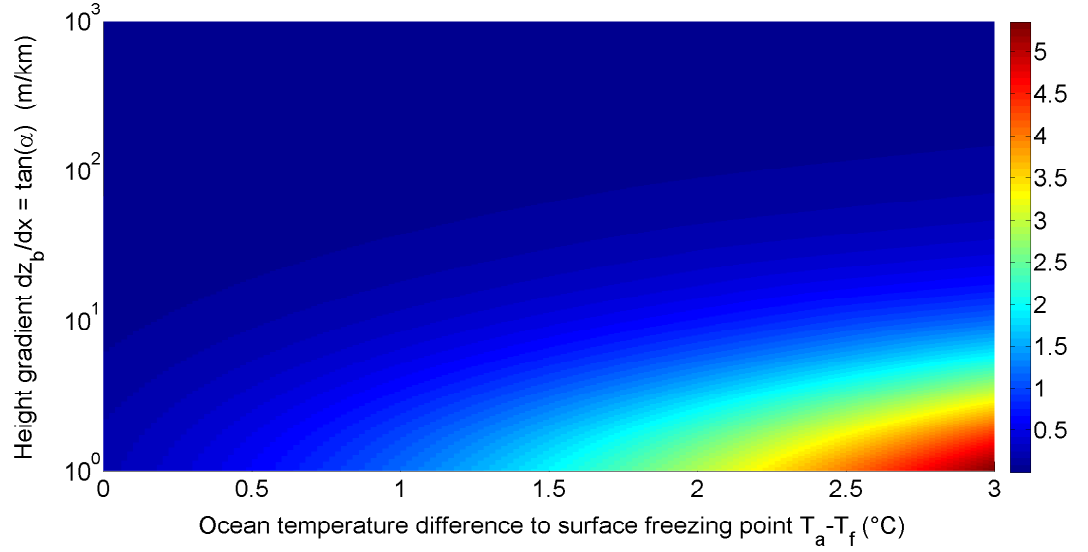


Figure 6.7: Sensitivity of maximum melt rate to changes in local slope $\frac{\partial \dot{m}}{\partial \alpha}$ (m/yr/(m/km)) (Figure 3.7d) for a logarithmic saturation of slope $\alpha_{eff} = \frac{\ln(1+1000\alpha)}{1000}$ (Figure 4.4a).

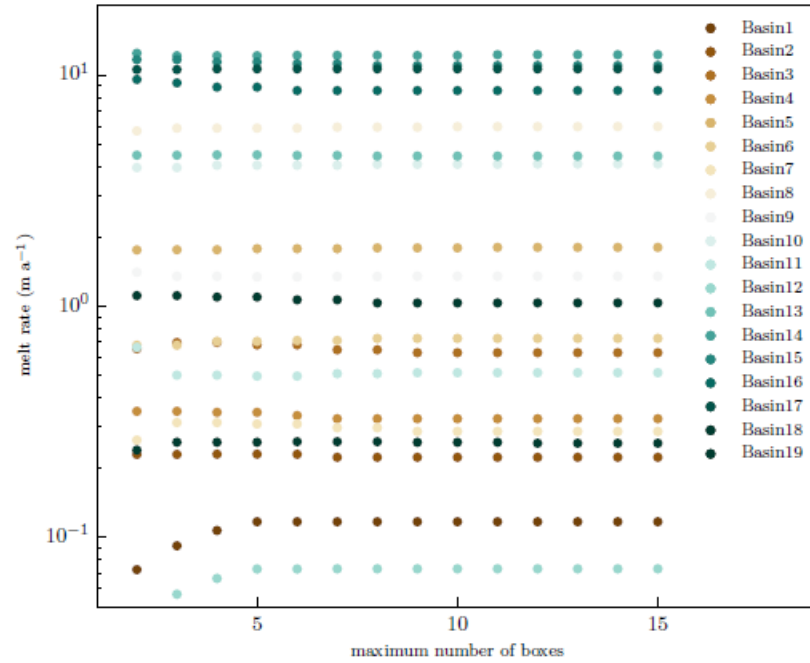


Figure 6.8: Sensitivity of mean sub-shelf melt rates to the maximum number of boxes of PICO. (Reese et al. (2018a), Supplementary Information

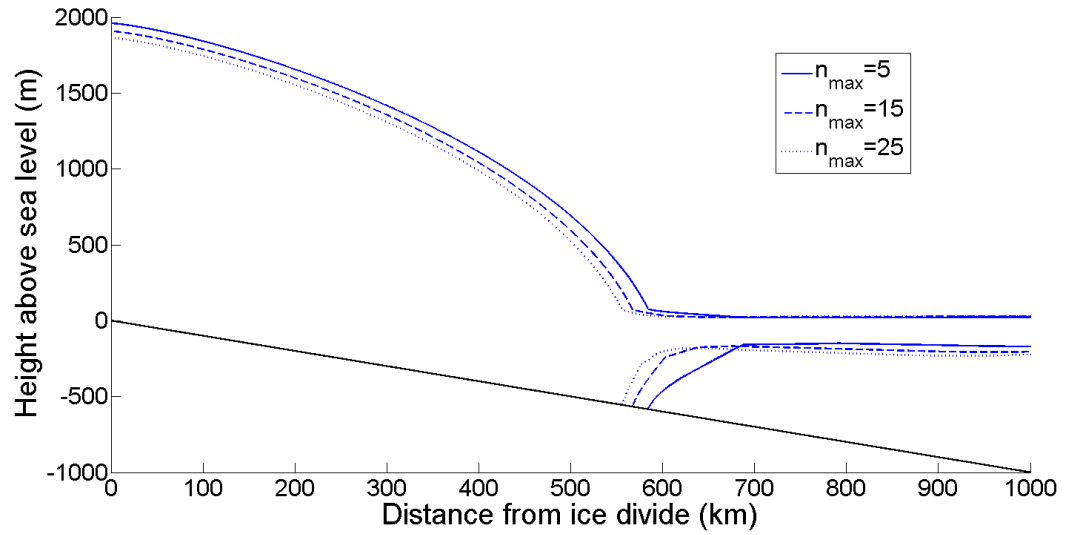


Figure 6.9: Grounding line migration due to varying maximum number of boxes n_{\max} in the box parametrization.

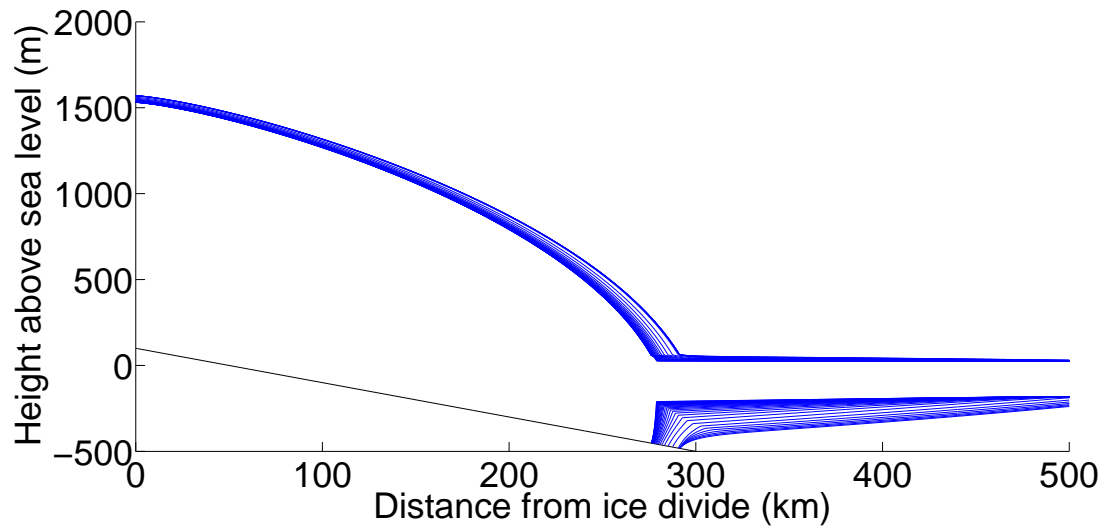


Figure 6.10: Shelf profiles for stepwise increase of ocean temperature for the plume parametrization (see section 5.2).

References

- Arzeno, I.B., Beardsley, R.C., Limeburner, R.Owens, B., Padman, L. , Springer, S.R., Stewart, C.L. and Williams, M.J.M. 2014. Ocean variability contributing to basal melt rate near the ice front of Ross Ice Shelf, Antarctica, *Journal of Geophysical. Research: Oceans*, 119, 4214-4233
- Beckmann, A. and Goosse, H. 2003. A parameterization of ice shelf?ocean interaction for climate models. *Ocean modelling*, 5, 157-170
- Bernales, J., Rogozhina, I., Thomas, M. 2017. Melting and freezing under Antarctic ice shelves from a combination of ice-sheet modelling and observations. *Journal of Glaciology*, 63, 731-744
- Carter, L., McCave, I.N. and Williams, M. 2009. Circulation and water masses of the Southern Ocean: A review. *Developments in Earth and Environmental Sciences*, 8, 85-114
- Craven, M., Allison, I., Fricker, H.A. and Warner, R. 2009. Properties of a marine ice layer under the Amery Ice Shelf, East Antarctica. *Journal of Glaciology*, 55, 717-728
- DeConto, R. M. and Pollard, D. 2016. Contribution of Antarctica to past and future sea-level rise, *Nature*, 531, 591-597
- De Rydt, J., Holland, P.R., Dutrieux, P. and Jenkins, A. 2014. Geometric and oceanographic controls on melting beneath Pine Island Glacier. *Journal of geophysical research: Oceans*, 119, 2420-2438
- Dinniman, M.S., X.S. Asay-Davis, B.K. Galton-Fenzi, P.R. Holland, A. Jenkins, and R. Timmermann. 2016. Modeling ice shelf/ocean interaction in Antarctica: A review. *Oceanography*, 29(4), 144-153
- Dutrieux, P., D. G. Vaughan, H. F. J. Corr, A. Jenkins, P. R. Holland, I. Joughin, and A. Fleming. 2013. Pine Island Glacier ice shelf melt distributed at kilometre scales, *Cryosphere*, 7(2), 1591-1620

Dutrieux, P., C. Stewart, A. Jenkins, K. W. Nicholls, H. F. J. Corr, E. Rignot, and K. Steffen. 2014. Basal terraces on melting ice shelves, *Geophysical research letters*, 41, 5506-5513

Favier, L., Durand, G., Cornford, S.L., Gudmundsson, G.H., Gagliardini, O., Gillet-Chaulet, F., Zwinger, T., Payner, A.J. and Le Brocq, A.M. 2014. Retreat of Pine Island Glacier controlled by marine ice-sheet instability. *Nature climate change*, 4, 117-121

Fyfe, J.C. and Saenko, O.A. 2005. Human-Induced Change in the Antarctic Circumpolar Current. *Journal of climate*, 18, 3068-3073

Gladstone, R.M, Payne, A.J. and Cornford, S.L. 2012. Resolution requirements for grounding-line modelling: sensitivity to basal drag and ice-shelf buttressing. *Annals of glaciology*, 53(60), 97-105

Gladstone, R.M., Walker, R.L., Galton-Fenzi, B.K., Gagliardini, O., Zwinger, T, and Greve, R. 2017. Marine ice sheet model performance depends on basal sliding physics and sub-shelf melting. *The Cryosphere*, 11, 319-329

Gudmundsson, G.H., Krug, J., Durand, G., Favier, L. and Gagliardini, O. 2012. The stability of grounding lines on retrograde slopes. *The Cryosphere*, 6, 1497-1505

Gudmundsson, G. Hilmar. 2013. Ice-shelf buttressing and the stability of marine ice sheets. *The Cryosphere*, 7, 647-655

Gwyther, D.E., Galton-Fenzi, B.K., Dinnima, M.S., Roberts, J.L. and Hunter, J.R. 2015. The effect of basal friction on melting and freezing in ice shelf-ocean models. *Ocean modelling*, 95, 38-52

Hattermann, T. and Levermann, A. 2010. Response of Southern Ocean circulation to global warming may enhance basal ice shelf melting around Antarctica. *Climate dynamics*, 35, 741-756

Hillenbrand, C.D., Smith, J.A., Hodell, D.A., Greaves, M., Poole, C.R., Kender, S., Williams, M., Anderson, T.J., Jernas, P.E., Elderfield, H., Klages, J.P., Roberts, S.J., Gohl, K., Larter, R.D. and Kuhn, G. 2017. West Antarctic Ice Sheet retreat driven by Holocene warm water incursions. *Nature*, 547, 43-48

Hindmarsh, R.C.A. 1993. Qualitative Dynamics of Marine Ice Sheets, in: *Ice in the Climate System*, 12, 67-99

Hindmarsh, R.C.A. 2006. The role of membrane-like stresses in determining the stability and

sensitivity of the antarctic ice-sheets: back-pressure and grounding-line motion. *Philosophical transactions of the Royal Society*, 364, 1733-1767

Hindmarsh, R.C.A. 2004, A numerical comparison of approximations to the Stokes equations used in ice sheet and glacier modeling. *Journal of Geophysical Research*, 109, F01012

Holland, D.M. and Jenkins, A. 1999. Modeling Thermodynamic Ice-Ocean Interactions at the Base of an Ice Shelf. *Journal of Physical Oceanography*, 29, 1787-1800

Holland, P.R and Feltham, D.L. 2006. The Effects of Rotation and Ice Shelf Topography on Frazil-Lade Ice Shelf Water Plumes. *Journal of physical oceanography*, 36, 2312-2327

Holland, P.R., Feltham, D.L. and Jenkins, A. 2007. Ice Shelf Water plume flow beneath Filchner-Ronne Ice Shelf, Antarctica. *Journal of geophysical research*, 112, C05044

Holland, P.R., Jenkins, A. and Holland, D.M. 2008. The Response of Ice Shelf Basal Melting to Variations in Ocean Temperature. *Journal of climate*, 21, 2558-2572

Holland, P.R., Corr, H.F., Vaughan, D.G. and Jenkins, A. 2009. Marine ice in Larsen Ice Shelf. *Geophysical Research Letters*, 36, L11604

Jacobs, S.S., Helmer, H.H., Doake, C.S., Jenkins, A. and Frolich, R.M. 1992. Melting of ice shelves and mass balance of Antarctica. *Journal of glaciology*, 38, 1992

Jacobs, S. S., A. Jenkins, C. F. Giulivi, and P. Dutrieux. 2011. Stronger ocean circulation and increased melting under Pine Island Glacier ice shelf, *Nature Geoscience*, 4, 519-523.

Jenkins, Adrian. 1991. One-Dimensional Model of Ice Shelf-Ocean Interaction. *Journal of Geophysical Research*, 96, 671-677

Jenkins, A. and Bombosch, A. 1995. Modeling the effects of frazil ice crystals on the dynamics and thermodynamics of Ice Shelf Water plumes. *Journal of Geophysical Research*, 100, 6967-6981

Jenkins, A., Nicholls, K.W., Corr, H.F. 2010. Observation and Parameterization of Ablation at the Base of Ronne Ice Shelf, Antarctica. *Journal of Physical Oceanography*, 40, 2298-2312

Jenkins, A., Shoosmith, D., Dutrieux, P., Jacobs, S., Kim, T.W., Lee, S.H., Ha, H.K. and Stammerjohn, S. West Antarctic Ice Sheet retreat in the Amundsen Sea driven by decadal oceanic variability. *Nature geoscience* (in press)

Jones, D.W. and Wells, A.J. 2018. Frazil-ice growth rate and dynamics in mixed layers and sub-ice-shelf plumes. *The Cryosphere*, 12, 25-38

Joughin, I., Smith, B.E. and Medley, B. 2014. Marine Ice Sheet Collapse Potentially Underway for the Thwaites Glacier Basin, West Antarctica. *Science*, 344, 735-738

Kader, B.A. and Yaglom, A.M. 1972. Heat and mass transfer laws for fully turbulent wall flows. *International Journal of Heat and Mass Transfer*, 15, 2329-2351

Lazeroms, W.M.J., Jenkins, A., Gudmundsson, G.H., van de Wall, R.S.W. 2018. Modelling present-day basal melt rates for Antarctic ice shelves using a parametrization of buoyant melt-water plumes. *The Cryosphere*, 12, 49-70

Makinson, K., Holland, P.R., Jenkins, A., Nicholls, K.W., and Holland, D.M. 2011. Influence of tides on melting and freezing beneath Filchner-Ronne Ice Shelf, Antarctica. *Geophysical Research Letters*, 38, L06601

Martin, M.A., Winkelmann, R., Haseloff, M., Albrecht, T., Bueler, E., Khroulev, C., Levermann, A. 2011. The Potsdam Parallel Ice Sheet Model (PISM-PIK) - Part 2: Dynamic equilibrium simulation of the Antarctic ice sheet. *The Cryosphere*, 5, 727-740

MacAyeal, Douglas. 1989. Large-Scale ice flow over a viscous basal sediment: theory and application to ice stream B, Antarctica. *Journal of geophysical research*, 94, 4071-4087

McPhee, Miles. 1992. Turbulent Heat Flux in the Upper Ocean Under Sea Ice. *Journal of Geophysical Research*, 97, 5365-5379

Oerter, H., Kipfstuhl, J., Determann, J., Miller, H., Wagenbach, D., Minikin, A., and Graf, W. 1992. Evidence for basal marine ice in the Filchner-Ronne ice shelf. *Letters to Nature*, 358, 399-401

Olbers, D. and Hellmer, H. 2010. A box model of circulation and melting in ice shelf caverns. *Ocean Dynamics*, 60, 141-153

Orsi, A.H., Withworth, T. and Nowlin, W.D. 1995. On the meridional extent and fronts of the Antarctic Circumpolar Current. *Deep-sea research I*, 42, 641-673

Orsi, A.H., Johnson, G.C. and Bullister, J.L. 1999. Circulation, mixing, and production of Antarctic Bottom Water. *Progress in Oceanography*, 43, 55-109

Parizek, B.R. and Walker, R.T. 2010. Implications of initial conditions and ice-ocean coupling for grounding-line evolution. *Earth and Planetary Science Letters*, 300, 351-358.

Pattyn, F., Huyghe, A., De Brabaner, S., and De Smedt, B. 2006. Role of transition zones in marine ice sheet dynamics. *Journal of Geophysical Research*, 111, F02004

Pattyn, F., Schoof, C., Perichon, L., Hindmarsh, R.C.A., Bueller, E., de Fleurian, B., Durand, G., Gagliardini, O., Gladstone, R., Goldberg, D., Gudmundsson, G.H., Huybrechts, P., Le, V., Nick, F.M., Payne, A.J., Pollard, D., Rybak, O., Saito, F. and Vieli, A. 2012. Results of the Marine Ice Sheet Model Intercomparison Project, MISMP. *The Cryosphere*, 6, 573-588

Pattyn, F., Perichon, L., Durand, G., Favier, L., Gagliardini, O., Hindmarsh, R.C.A., Zwinger, T., Albrecht, T., Cornford, S., Docquier, D., Fürst, J.J., Goldberg, D., Gudmundsson, H., Humbert, A., Hütten, M., Huybrechts, P., Jouvét, G., Kleiner, T., Larour, E., Martin, D., Mortlighem, M., Payne, A.J., Pollard, D., Rückamp, M., Rybak, O., Seroussi, H., Thoma, M. and Wilkens, N. 2013. Grounding-line migration in plan-view marine ice-sheet models: results of the ice2sea MISMP3d intercomparison. *Journal of glaciology*, 59, 410-422

Pattyn, Frank. 2017. Sea-level response to melting of Antarctic ice shelves on multi-centennial time scales with the fast Elementary Thermomechanical Ice Sheet model (f.ETISh v1.0). *The Cryosphere Discuss.*, 11, 1851-1878

Payne, A. J., P. R. Holland, A. P. Shepherd, I. C. Rutt, A. Jenkins, and I. Joughin. 2007. Numerical modeling of ocean-ice interactions under Pine Island Bay's ice shelf. *Journal of Geophysical Research*, 112, C10019

Petty, A.A., Feltham, D.L. and Holland, P.R. 2013. Impact of Atmospheric Forcing on Antarctic Continental Shelf Water Masses. *Journal of physical oceanography*, 43, 920-940

Pollard, D. and DeConto, R.M. 2012a. Description of a hybrid ice sheet-shelf model, and application to Antarctica. *Geoscience Model Development*, 5, 1273-1295

Pollard, D., DeConto, R.M. and Alley, R.B. 2015. Potential Antarctic Ice Sheet retreat driven by hydrofracturing and ice cliff failure. *Earth and Planetary Science Letters*, 412, 112-121

Press, W., S. Teukolsky, W. Vetterling, and B. Flannery. 1992. *Numerical Recipes in C: The Art of Scientific Computing*. 2nd ed., 994 pp., Cambridge University Press, New York.

Reese, R., Albrecht, T., Mengell, M., Asay-Davis, X., Winkelmann, R. 2018a. Antarctic sub-shelf melt rates via PICO. *The Cryosphere Discussion*, 12, 1969-1985

Reese, R., Gudmundsson, G.H., Levermann, A. and Winkelmann, R. 2018b. The far reach of ice-shelf thinning in Antarctica. *Nature Climate Change*, 8, 53-57

- Rignot, E., Jacobs, S., Mouginot, J., and Scheuch, B. 2013. Ice-shelf melting around Antarctica, *Science*, 341, 266-270
- Rignot, E., Mouginot, J., Morlighem, M., Seroussi, H. and Scheuchl, B. 2014. Widespread, rapid grounding line retreat of Pine Island, Thwaites, Smith, and Kohler glaciers, West Antarctica, from 1992 to 2011. *Geophysical research letters*, 41, 3502-3509
- Rommelaere, V. and Ritz, C. 1996. A thermomechanical model of ice-shelf flow. *Annals of glaciology*, 23, 13-20
- Thoma, M., Jenkins, A., Holland, D. and Jacobs, S. 2008. Modelling Circumpolar Deep Water intrusions on the Amundsen Sea continental shelf, Antarctica. *Geophysical research letters*, 35, L18601
- Thomas, R. 1979. The dynamics of marine ice sheets. *Journal of glaciology*, 24, 167-177
- Turner, J., A. Orr, G. H. Gudmundsson, A. Jenkins, R. G. Bingham, C.-D. Hillenbrand, and T. J. Bracegirdle. 2017. Atmosphere-ocean-ice interactions in the Amundsen Sea Embayment, West Antarctica. *Reviews of geophysics*, 55, 235-276
- Van der Veen, C. J. and I.M. Whillans. 1996. Model experiments on the evolution and stability of ice streams. *Annals of glaciology*, 23, 129-137
- Vieli, A. and Payne, A.J. 2003. Application of control methods for modelling the flow of Pine Island Glacier, West Antarctica. *Ann. Gl.*, 36, 197-204
- Vieli, A. and Payne, A.J. 2005. Assessing the ability of numerical ice sheet models to simulate grounding line migration. *Journal of geophysical research*, 110, F01003
- Walker, R.T. and Holland, D.M. 2007. A two-dimensional coupled model for ice shelf-ocean interaction. *Ocean modelling*, 17, 123-139
- Walker, R.T., Dupont, T.K., Parizek, B.R. and Alley, R.B. 2008. Effects of basal-melting distribution on the retreat of ice-shelf grounding lines. *Geophysical Research Letters*, 35, L17503
- Weertman, Johannes. 1974. Stability of the junction of an ice sheet and an ice shelf. *Journal of glaciology*, 13, 3-11
- Weertman, Johannes. 1983. Creep deformation of ice. *Annual Reviews of Earth and Planetary Sciences*, 11, 215-240

Winkelmann, R., Martin, M.A., Haseloff, M., Albrecht, T., Bueler, E., Khroulev, C., Levermann, A. 2010. The Potsdam Parallel Ice Sheet Model (PISM-PIK) - Part 1: Model description. *The Cryosphere*, 5, 715-726